Synchronous tropical and polar temperature evolution in the Eocene

Margot J. Cramwinckel[1]*, Matthew Huber[2], Ilja J. Kocken[1], Claudia Agnini[3], Peter K. Bijl[1], Steven M. Bohaty[4], Joost Frieling[1], Aaron Goldner[2], Frederik J. Hilgen[1], Elizabeth L. Kip[1], Francien Peterse[1], Robin van der Ploeg[1], Ursula Röhl[5], Stefan Schouten[1,6], Appy Sluijs[1]

*m.j.cramwinckel@uu.nl

[1] Department of Earth Sciences, Faculty of Geoscience, Utrecht University, Utrecht, The Netherlands

[2] Department of Earth, Atmospheric, and Planetary Sciences, Purdue University, West Lafayette, United States

[3] Department of Geosciences, University of Padova, Padova, Italy

[4] Ocean and Earth Science, National Oceanography Centre Southampton, University of Southampton, Southampton, United Kingdom

[5] MARUM Center for Marine Environmental Sciences, University of Bremen, Bremen, Germany

[6] NIOZ Royal Netherlands Institute for Sea Research, Department of Marine Microbiology and Biogeochemistry, Den Burg, Texel, The Netherlands

Understanding derived from palaeoclimate reconstructions of periods with warm climates and high atmospheric pCO_2 is crucial for developing better projections of future climate change. Deep-ocean[1,2] and high-latitude[3] palaeotemperature proxies demonstrate that the Eocene (56–34 million years ago; Ma) encompasses the warmest interval of the past 66 million years, which is followed by cooling towards eventual establishment of ice-caps on Antarctica. As Eocene polar warmth is well established, the main obstacle in quantifying evolution of key climate parameters, such as global average temperature change and its polar amplification, is a lack of continuous high-quality tropical temperature reconstructions. Here we present the first continuous Eocene equatorial sea surface temperature record, based on biomarker palaeothermometry applied on Atlantic Ocean sediments (Ocean Drilling Program Site 959). We compile this new record with the sparse existing data[4–6] to construct a 26-Myr multi-proxy, multi-site stack of Eocene tropical climate evolution. We find that tropical and deep-ocean temperatures changed in parallel, over both long-term climate trends and short-lived events. This is consistent with the hypothesis that greenhouse gas forcing[7,8] rather than changes in ocean circulation[9,10] was the main driver of Eocene climate. Moreover, there is a strong linear relationship between tropical and deep-ocean temperatures, implying a constant polar amplification factor throughout the generally ice-free Eocene. Quantitative comparison with fully-coupled climate model simulations indicates that global average temperatures were ~29ºC, 26°C, 23ºC and 19ºC in the early, early-middle, late-middle and late Eocene, respectively, compared to a preindustrial 14.4ºC. Finally, combining proxy- and model-based temperature estimates with available CO_2

reconstructions[8] yields estimates of Eocene Earth System Sensitivity of 0.9–2.3 K W^{-1} m^{-2} at 68% probability, consistent with the high end of previous estimates[11].

It is well established that deep-ocean temperatures peaked during the Early Eocene Climatic Optimum (EECO; ~52–50 Ma) and had declined substantially by the latest Eocene (~34 Ma)[1,2]. These trends are mimicked in sea surface temperature (SST) reconstructions from the southern high latitudes[3] as Eocene deep-ocean temperatures reflect Southern Ocean winter surface conditions that are relayed to the abyss through deep-water formation[12]. However, to unlock the unique promise of Eocene palaeoclimate records to answer fundamental questions about the relationship between pCO_2 and global temperature, and to quantify polar amplification of climate change, accurate reconstructions of tropical surface oceans are required. Moreover, tropical records are necessary to test the two competing hypotheses for Eocene deep-ocean and polar cooling: (1) decreasing greenhouse gas concentrations, CO_2 predominantly[7,8], and (2) changes in ocean circulation and meridional heat transport associated with opening of ocean gateways[9,10]. Gateway opening cools the Southern and deep-ocean while warming the upper tropical ocean by a few degrees[13], whereas CO_2 decline leads to global cooling at both the equator and the poles[14] – albeit with predicted amplified polar temperature change relative to the tropics[15]. Importantly, this amplification factor affects ice sheet volume and extent and therefore global sea level, and is therefore critical to constrain, also for future projections. Yet, despite evidence for CO_2 decline over the Eocene[8], existing tropical records[4–6] are fragmentary and of low resolution and therefore insufficient to address these crucial questions.

We generated new temperature reconstructions from a clay-bearing, micritic porcellanite sequence recovered at Ocean Drilling Program Site 959 in the eastern equatorial Atlantic Ocean (**Figure 1**). Site 959 was positioned at near-equatorial latitudes and deep bathyal water depths throughout the Eocene[16] (**Extended Data Table 1a**). We augment the existing age-model[16] with new biostratigraphic and chemostratigraphic constraints (**Extended Data Table 1b**, **Extended Data Figure 1**). While carbonate preservation is poor[16], well-preserved, immature organic matter is present throughout[17]. We therefore employ the organic TEX_{86} palaeothermometer to reconstruct SST. TEX_{86} utilizes the temperature-dependent distribution of thaumarchaeotal membrane lipids. Fractional abundances of the various lipids at Site 959 indicate an upper water column (50–300 m) source (**Methods**), which allows confident SST interpretations from TEX_{86}. Several calibrations exist to translate TEX_{86} into SST based on a modern core-top data set[18]. For biophysical and analytical reasons, we prefer conservative estimates of tropical temperature generated by the logarithmic TEX_{86}^{H} calibration[18] (**Methods, Extended Data Figure 2**). In addition, we use the linear BAYSPAR calibration[19] as a complementary analysis (**Extended Data Figure 3**).

Our new equatorial record from Site 959 (**Figure 2**) shows latest Palaeocene (~58 to 56 Ma) SSTs of 31–33ºC, mimicking time-equivalent SSTs derived from glassy-preserved planktonic foraminiferal $\delta^{18}O$ and Mg/Ca ratios, and TEX_{86}^{H} from a nearby section in Nigeria[20] – supporting the notion that TEX_{86}^{H} accurately reflects SST at Site 959. The record further reveals 2–3ºC of latest Palaeocene to earliest Eocene (58 to 53 Ma) warming to peak EECO temperatures of 34–35ºC. Superimposed transient ~4ºC warming to ~37ºC occurred during the Palaeocene-Eocene Thermal Maximum

95 (PETM) at ~56 Ma[21]. A long-term ~7ºC SST drop to ~28ºC characterises the middle
96 to late Eocene interval, and an additional ~2ºC of cooling to ~26ºC marks the Eocene-
97 Oligocene transition (at ~34 Ma). Superimposed on long-term cooling is the first
98 tropical SST reconstruction of the Middle Eocene Climatic Optimum[22] (MECO) at
99 ~40 Ma, displaying a ~4ºC warming from background temperatures to a peak of
100 ~33ºC. This provides compelling evidence that the MECO was associated with global
101 warming; surface warming was previously only recognized in extratropical regions of
102 the Southern Hemisphere. We also record pre-MECO temperature variability of
103 similar duration but lesser amplitude.
104
105 To assess if regional upwelling at Site 959[(17)] influenced TEX_{86}-based SST variability,
106 we consider published total organic carbon (TOC) contents[17] and generate dinocyst
107 assemblage data, as dinocysts are highly sensitive to upwelling in modern and
108 Palaeogene oceans[23] (**Extended Data Figure 4**). The continuous presence of
109 Protoperidiniaceae (derived from heterotrophic dinoflagellates) and elevated TOC
110 within biosiliceous sediments[16] indicate upwelling throughout the middle and late
111 Eocene. The early Eocene is less well constrained but presence of Protoperidiniaceae
112 and abundant biosilica suggest upwelling. An upper Eocene increase in TOC content[17]
113 might indicate upwelling intensification. Although this may exaggerate latest Eocene
114 cooling at Site 959, the recorded magnitude (~2ºC) is similar to previous work at
115 tropical locations[24] (**Figure 2**). Apart from the late Eocene, however, variations in our
116 SST record are not strongly correlated to changes in the abundance of upwelling-
117 indicative dinocysts or TOC content. Regional upwelling may have muted SSTs by a
118 few degrees. Indeed, our values are somewhat lower than the few time-equivalent data
119 points from the warm pool sampled in Tanzania[4], suggesting we for the first time

sampled the Eocene analogue to the 'cold tongue' in the modern ocean. Importantly, however, this analysis indicates that variations in the strength of upwelling were not a major factor governing SST change at the study site.

We combine our equatorial Site 959 SST record with the available low-resolution data from a suite of SST proxies from the Indian, Atlantic, and Pacific tropical oceans (**Figure 2,** data sources in **Extended Data Figure 5**). Each of these proxies is subject to different systematic sources of error, thus the close correspondence in both absolute temperatures and trends between various organic and carbonate proxies indicates a robust convergent temperature signal. A LOESS model is applied to the resulting compilation to produce an estimate of Eocene mean tropical temperature (**Figure 3a**), yielding 4–7ºC of cooling through the Eocene. Remarkably, long-term trends and sub-Myr (MECO and PETM) tropical SST variations mimic those from the Southern Ocean and the deep-ocean, based on an updated compilation of benthic foraminifer $\delta^{18}O$-derived temperatures (**Figure 2**). A sensitivity study indicates that potential late Eocene Antarctic ice caps did not appreciably affect this deep-ocean temperature proxy (**Methods, Extended Data Figure 6**). The close correspondence between tropical and deep-sea temperatures provides solid proof that greenhouse gas forcing rather than ocean circulation change caused Eocene cooling, as suggested elsewhere[5,7,8].

As an approximation of the pole-to-equator temperature difference, or meridional temperature gradient (MTG), we calculate the difference between tropical mean SST and deep-ocean temperatures (**Methods, Figure 3b**). Although different TEX_{86} calibrations result in slightly different early Eocene MTGs (**Extended Data Figure**

145 **3**), the gradient generally increases with cooling climate and vice versa, reflecting
146 polar amplification of temperature variability. Remarkably, regression analysis
147 indicates a strong linear relationship between deep-ocean and tropical temperatures
148 (**Figure 4a**; also between high latitude and tropical SST **Extended Data Figure 7**).
149 Although uncertainty on the exact value is large due to uncertainties in temperature
150 proxies and calibrations (**Figure 4b; Extended Data Figure 3**), this signifies a stable
151 polar amplification factor throughout the Eocene. As the obtained values are
152 consistent with polar amplification derived from a spatially better resolved analysis
153 for the PETM event[20], this seems true for both short (10^5 yr) and long (multi-million
154 yr) timescales. In the absence of pronounced snow and ice albedo feedbacks, the polar
155 amplification factor should be determined by atmospheric feedbacks[25]. Therefore,
156 importantly, the stable amplification factor implies that the strength of these
157 feedbacks scales linearly with temperature in an ice-free world.
158
159 Our temperature proxy compilations provide a concrete and robust test of the ability
160 of models to reproduce past warm climates under increased greenhouse gas forcing.
161 We have performed fully-coupled general circulation model simulations using the
162 NCAR Community Earth System Model version 1 (CESM 1) applying a range of
163 radiative forcings equivalent to a range of Eocene CO_2 concentrations (560, 1120,
164 2240 and 4480 ppm; simulations EO1–EO4, respectively) run to full equilibrium. The
165 close correspondence between tropical, high latitude and deep sea temperature trends
166 (**Figure 2**) supports model-based inferences that Eocene global mean temperature was
167 relatively insensitive to variations in palaeogeography[7,13,26], so we did not vary
168 palaeogeographic boundary conditions. The modelled deep waters derive primarily
169 from polar surface waters[12], justifying our use of the modelled and proxy-derived

vertical gradient as an approximation for the MTG. The four simulations EO1–EO4 were associated with specific age ranges by matching the simulated deep-ocean temperatures to the proxy-based deep-ocean temperatures, thus leaving SST as the predicted variable. Crucially, the simulations closely approximate the multi-proxy, multi-location tropical SST compilation for these four time slices (**Figure 3a**). Therefore, the Eocene temperature gradients of 19–26ºC as reconstructed from proxies are also closely reproduced (**Figure 3b**). This implies that current-generation climate models are capable of resolving the "low temperature gradient problem"[14] of Eocene greenhouse climates provided sufficient forcing, albeit with two important exceptions. First, regional proxy-model data mismatches for absolute temperatures in the South Pacific[12] and Arctic[27] Oceans remain a conundrum, which this study does not resolve. Second, the model simulations do not fully reproduce the most reduced proxy-derived gradients of the early Eocene. Based on recent modelling experiments with tuned cloud parameters[28], one potential explanation could be that the early Eocene hothouse experienced different cloud behaviour and shortwave radiative feedbacks (simulation EO_CP in **Figure 3b**). This simulation with tuned clouds produces a more reduced early Eocene MTG at lower pCO_2, but those same parameters lead to a poorer simulation of the MTG during the PETM[28] (**Extended Data Figure 8**), indicating that this remains an unresolved problem.

With the overall excellent match between ocean temperature proxy reconstructions and model simulations, we can use the latter to estimate global mean temperatures, required to calculate climate sensitivity to CO_2 forcing. Global mean temperatures were 29ºC, 26ºC, 23ºC and 19ºC during the early (54–49 Ma), early middle (48–46 Ma), late middle (42–41 Ma), and late Eocene (38–35 Ma), respectively, compared to

195 a preindustrial temperature of 14.4ºC. These may be slightly underestimated if South
196 Pacific[3,12] and Arctic[27] temperature reconstructions represent accurate estimates of
197 annually averaged SST. Crucially, however, our model requires much larger changes
198 in CO_2 to produce the large and dynamic range of Eocene tropical SST and deep sea
199 temperature than reconstructed from proxy data[8]. This implies that the emergent Earth
200 System Sensitivity[11] (ESS) to doubling of pCO_2 of 3.5°C in the model is too low to
201 create sufficient warmth. We consider available Eocene CO_2 reconstructions[8] in
202 combination with our proxy- and model-based temperatures (**Methods**) to estimate
203 ESS between the various parts of the Eocene (**Extended Data Figure 9**). Our
204 probabilistic analysis for the early to late Eocene cooling results in a calculated proxy-
205 based ESS range of 0.9–2.3 K W^{-1} m^{-2} (68% highest density interval; equivalent to
206 3.5–8.9°C per pCO_2 doubling) consistent with the high end of previous estimates[11].
207
208 The large range of Eocene tropical temperatures on both short and long timescales
209 indicates that the tropics respond strongly to changes in greenhouse gases even at high
210 temperatures. In addition to high absolute temperatures of up to ~35ºC and ~37ºC
211 during the EECO and PETM[21], respectively, this refutes the notion of stable tropical
212 temperatures[4], kept constant through a physical "thermostat" mechanism[29]. Moreover,
213 our results show that tropical SST varied in tandem with high-latitude and deep-ocean
214 temperatures, with a stable Eocene polar amplification factor, consistent with a
215 dominant role of CO_2 forcing in both long-term Eocene climate evolution and
216 superimposed aberrations including the PETM and MECO. Tropical temperatures are
217 expected to rise in response to anthropogenic greenhouse gas emissions. Given the
218 consistency between our climate simulations and reconstructions, current-generation
219 fully-coupled climate models are likely to perform adequately in predicting future

220 tropical SST change, although accurate determination of the sensitivity of global
221 climate to CO_2 change remains a major challenge.
222

Main references

1. Lear, C. H., Elderfield, H. & Wilson, P. A. Cenozoic Deep-Sea Temperatures and Global Ice Volumes from Mg/Ca in Benthic Foraminiferal Calcite. *Science* **287,** 269–272 (2000).
2. Zachos, J. C., Dickens, G. R. & Zeebe, R. E. An early Cenozoic perspective on greenhouse warming and carbon-cycle dynamics. *Nature* **451,** 279–283 (2008).
3. Bijl, P. K. *et al.* Early Palaeogene temperature evolution of the southwest Pacific Ocean. *Nature* **461,** 776–779 (2009).
4. Pearson, P. N. *et al.* Stable warm tropical climate through the Eocene Epoch. *Geology* **35,** 211–214 (2007).
5. Inglis, G. N. *et al.* Descent toward the Icehouse: Eocene sea surface cooling inferred from GDGT distributions. *Paleoceanography* **30,** 2014PA002723 (2015).
6. Evans, D. *et al.* Eocene greenhouse climate revealed by coupled clumped isotope-Mg/Ca thermometry. *Proc. Natl. Acad. Sci.* 201714744 (2018). doi:10.1073/pnas.1714744115
7. Huber, M. *et al.* Eocene circulation of the Southern Ocean: Was Antarctica kept warm by subtropical waters? *Paleoceanography* **19,** PA4026 (2004).
8. Anagnostou, E. *et al.* Changing atmospheric CO2 concentration was the primary driver of early Cenozoic climate. *Nature* **533,** 380–384 (2016).
9. Kennett, J. P. Cenozoic evolution of Antarctic glaciation, the circum-Antarctic Ocean, and their impact on global paleoceanography. *J. Geophys. Res.* **82,** 3843–3860 (1977).
10. Bijl, P. K. *et al.* Eocene cooling linked to early flow across the Tasmanian Gateway. *Proc. Natl. Acad. Sci.* **110,** 9645–9650 (2013).

11. PALAEOSENS Project Members. Making sense of palaeoclimate sensitivity. *Nature* **491,** 683–691 (2012).
12. Hollis, C. J. *et al.* Early Paleogene temperature history of the Southwest Pacific Ocean: Reconciling proxies and models. *Earth Planet. Sci. Lett.* **349–350,** 53–66 (2012).
13. Sijp, W. P., England, M. H. & Huber, M. Effect of the deepening of the Tasman Gateway on the global ocean. *Paleoceanography* **26,** PA4207 (2011).
14. Huber, M. & Caballero, R. The early Eocene equable climate problem revisited. *Clim. Past* **7,** 603–633 (2011).
15. Lunt, D. J. *et al.* A model–data comparison for a multi-model ensemble of early Eocene atmosphere–ocean simulations: EoMIP. *Clim Past* **8,** 1717–1736 (2012).
16. Mascle, J., Lohmann, G. P., Clift, P. D. & Shipboard Scientific Party. *Proceedings of the Ocean Drilling Program Initial Reports*. **159,** (1996).
17. Wagner, T. Late Cretaceous to early Quaternary organic sedimentation in the eastern Equatorial Atlantic. *Palaeogeogr. Palaeoclimatol. Palaeoecol.* **179,** 113–147 (2002).
18. Kim, J.-H. *et al.* New indices and calibrations derived from the distribution of crenarchaeal isoprenoid tetraether lipids: Implications for past sea surface temperature reconstructions. *Geochim. Cosmochim. Acta* **74,** 4639–4654 (2010).
19. Tierney, J. E. & Tingley, M. P. A Bayesian, spatially-varying calibration model for the TEX86 proxy. *Geochim. Cosmochim. Acta* **127,** 83–106 (2014).
20. Frieling, J. *et al.* Extreme warmth and heat-stressed plankton in the tropics during the Paleocene-Eocene Thermal Maximum. *Sci. Adv.* **3,** e1600891 (2017).

21. Frieling, J. *et al.* Tropical Atlantic climate and ecosystem regime shifts during the Paleocene–Eocene Thermal Maximum. *Clim Past* **14,** 39–55 (2018).

22. Bohaty, S. M., Zachos, J. C., Florindo, F. & Delaney, M. L. Coupled greenhouse warming and deep-sea acidification in the middle Eocene. *Paleoceanography* **24,** PA2207 (2009).

23. Sluijs, A., Pross, J. & Brinkhuis, H. From greenhouse to icehouse; organic-walled dinoflagellate cysts as paleoenvironmental indicators in the Paleogene. *Earth-Sci. Rev.* **68,** 281–315 (2005).

24. Liu, Z. *et al.* Global Cooling During the Eocene-Oligocene Climate Transition. *Science* **323,** 1187–1190 (2009).

25. Caballero, R. & Langen, P. L. The dynamic range of poleward energy transport in an atmospheric general circulation model. *Geophys. Res. Lett.* **32,** L02705 (2005).

26. Goldner, A., Herold, N. & Huber, M. Antarctic glaciation caused ocean circulation changes at the Eocene-Oligocene transition. *Nature* **511,** 574–577 (2014).

27. Sluijs, A. *et al.* Warm and wet conditions in the Arctic region during Eocene Thermal Maximum 2. *Nat. Geosci.* **2,** 777–780 (2009).

28. Kiehl, J. T. & Shields, C. A. Sensitivity of the Palaeocene–Eocene Thermal Maximum climate to cloud properties. *Philos. Trans. R. Soc. Lond. Math. Phys. Eng. Sci.* **371,** 20130093 (2013).

29. Pierrehumbert, R. T. Thermostats, Radiator Fins, and the Local Runaway Greenhouse. *J. Atmospheric Sci.* **52,** 1784–1806 (1995).

30. Matthews, K. J. *et al.* Global plate boundary evolution and kinematics since the late Paleozoic. *Glob. Planet. Change* **146,** 226–250 (2016).

Supplementary Information

Supplementary Table 1 | Calcareous nannofossil counts.

See Supplementary Data Excel file.

Supplementary Table 2 | Fractional abundances of isoprenoid GDGTs.

See Supplementary Data Excel file.

Supplementary Table 3 | Relative and absolute abundance of upwelling-indicative dinocysts.

See Supplementary Data Excel file.

Supplementary Table 4 | Selected temperature output of CESM simulations EO1-EO4 and EO_CP.

See Supplementary Data Excel file.

Supplementary Table 5 | Eocene tropical sea surface temperature compilation

See Supplementary Data Excel file.

Acknowledgements

This research used samples and data provided by the International Ocean Discovery Program (IODP) and its predecessor the Ocean Drilling Program. This work was carried out under the program of the Netherlands Earth System Science Centre (NESSC), financially supported by the Dutch Ministry of Education, Culture and Science. AS thanks the European Research Council (ERC) under the European Union Seventh Framework Program for ERC Starting Grant #259627. This study was made possible by NWO grant #834.11.006, which enabled the purchase of the UHPLC-MS system used for GDGT analyses. PKB and FP acknowledge NWO-ALW Veni Grants #863.13.002 and #863.13.016, respectively. MH was funded by the U.S. National Science Foundation grant OCE-0902882 and the CESM model is also supported by NSF. CA acknowledges University of Padova grant #BIRD161002. We thank Bridget Wade (University College London) for converting the Eocene TDP data to GTS2012, Phil Sexton (The Open University) for converting the middle Eocene Site 1258 data to GTS2012, Gert-Jan Reichart (Royal NIOZ and Utrecht University) for discussions, Luuk van der Heijden (Utrecht University, now at University of La Rochelle, France), Mike Nicolai (Utrecht University), Anchelique Mets (NIOZ), Natasja Welters, Arnold van Dijk and Dominika Kasjaniuk (Utrecht Geolab) for analytical support.

Author contributions

M.J.C., A.S., and M.H. designed the study. M.J.C., F.P., S.S., I.J.K., J.F. and E.L.K. generated and/or analyzed organic geochemical data. M.J.C., A.S., P.K.B., J.F., I.J.K. and E.L.K. generated and/or analyzed palynological data. C.A. generated and analyzed nannofossil data. I.J.K., F.H., C.A., J.F., R.v.d.P. and M.J.C. developed the age model. M.H. and A.G. performed CESM model simulations. All authors

contributed to data and/or model interpretations. M.J.C., A.S. and M.H. wrote the text, with input from all authors.

Competing financial interests

The authors declare no competing financial interests.

Materials & Correspondence

Correspondence and material requests should be addressed to M. J. Cramwinckel (m.j.cramwinckel@uu.nl).

Main figure legends

Figure 1 | Palaeogeographic reconstruction of 40 million years ago showing the approximate palaeoposition of the studied site (ODP Site 959) and the main sites we use for producing a tropical SST compilation (ODP Site 865, 925, and 929; Tanzania Drilling Project TDP; Sagamu Quarry SQ and IB10B Core, Nigeria). Continental plates shown in dark grey. Light grey gridlines represent latitudes and longitudes with 30º spacing. Map generated with GPlates, using the rotation frame and tectonic reconstruction of Matthews *et al.*[30].

Figure 2 | Eocene global climate evolution. a, CO_2 record from boron isotopes from TDP (squares; 68% confidence intervals as uncertainty) and alkenones from ODP Sites 612 and 925 (circles; uncertainties from original studies); data sources in **Methods**. **b,** Site 959 TEX_{86}^{H}-based SST (ºC) record (red) and additional tropical compilation (pink; see **ED Figure 5**). Dashed line represents a hiatus. Green diamonds (Site 1172) are high latitude TEX_{86}^{H}-based SST (ºC) record[3]. **c,** $\delta^{18}O$-based ice-free deep-ocean temperature (compiled in **Methods)**, with fitted LOESS model (black line), and 95% confidence interval (dark shading). Age follows GTS2012. Pal. = Palaeocene, Olig. = Oligocene.

Figure 3 | Proxy-model synthesis of Eocene temperatures. a, Top: tropical SST compilation (red) and LOESS model (black line) with 95% confidence interval (gray shading). Bottom: deep ocean temperatures from Fig. 2c. Open squares are mean modelled tropical SST and deep ocean temperature of simulations EO1 (560 ppm CO_2), EO2 (1120), EO3 (2240), and EO4 (4480) and EO_CP[28]; errors represent

seasonal range. Yellow shadings illustrate age ranges simulations are matched to. **b**, Calculated meridional temperature gradient based on LOESS fits of proxy data (line, propagated 95% confidence intervals) and model simulations EO1-4 and EO_CP (as in 3a). Age follows GTS2012. Pal. = Palaeocene, Olig. = Oligocene.

Figure 4 | Linear relationship between deep-ocean and tropical sea surface temperature. a, Proxy data (58-34 Ma in 1-Myr bins; errors are 1 stdev due to binning) and model results (open squares are model means for tropical compilation locations) of deep-ocean temperature against tropical SST. Slopes of Deming regressions (lines) represent polar amplification factor (□ 1 SE). The Site 959 55-56 Myr bin falls to the right of the regression line, because it includes much PETM data for Site 959 but less for the deep ocean. **b**, Density function of polar amplification factor with full propagation of errors (**Methods**) with hatched 68% highest density intervals.

Methods

Palynology

Freeze-dried sediments (96 samples) were crushed and treated with 30% HCl and twice with 38–40% HF to remove carbonates and silicates, respectively, after a known amount of *Lycopodium* spores (batch *no*. 1031, 20848 spores per tablet) was added to enable absolute quantification of palynomorphs. The 15–250 μm fraction was isolated using nylon mesh sieves and an ultrasonic bath. No oxidation procedure was applied. An aliquot of homogenized residue was mounted on slides and analysed using light microscopy (400x magnification) to a minimum of 200 identified dinocysts.

Organic geochemistry

Lipids were extracted from freeze-dried and powdered sediments (5–25 g dry weight, 118 samples) with dichloromethane (DCM):methanol (MeOH) (9:1, v:v) using a Dionex accelerated solvent extractor (ASE 350) at a temperature of 100°C and a pressure of 7.6×10^6 Pa. Lipid extracts were separated into an apolar, ketone and polar fraction by Al_2O_3 column chromatography using hexane:DCM (9:1), hexane:DCM (1:1), and DCM:MeOH (1:1), as respective eluents. 99 ng of a synthetic C_{46} (*m/z* 744) glycerol dialkyl glycerol tetraether (GDGT) standard was added to the polar fraction, which subsequently was dissolved in hexane:isopropanol (99:1, v/v) to a concentration of ~3 mg/mL and passed through a 0.45 μm polytetrafluoroethylene (PTFE) filter. This fraction was then analysed by high performance liquid chromatography/atmospheric pressure chemical ionization-mass spectrometry (HPLC/APCI-MS) using an Agilent 1260 Infinity series HPLC coupled to an Agilent 6130 single quadrupole MS at Utrecht University following Hopmans *et al.*[31] to

measure the abundance of GDGTs. Branched versus Isoprenoid Tetraether (BIT) index and TEX_{86} values were calculated according to Hopmans *et al.*[32] and Kim *et al.*[18], respectively. Based on long-term observation of the in-house standard, analytical precision for TEX_{86} is ± 0.3°C.

Glycerol Dialkyl Glycerol Tetraether (GDGT) distributions

Of the 118 samples analysed for GDGTs, 5 Early Eocene samples did not yield sufficient concentrations of GDGTs to determine TEX_{86}. Additionally, 4 samples were excluded because either GDGT-2 (2 samples) or crenarchaeol (2 samples) could not be reliably identified. For the remaining 109 samples we evaluated the sources of GDGTs and the reliability of TEX_{86}. The branched and isoprenoid tetraether (BIT) index[32], a means of quantifying the relative abundance of soil- and river-derived GDGTs relative to marine GDGTs, is low throughout the entire Eocene (all <0.25, with 90% of values <0.07) and there is no significant correlation between BIT index and TEX_{86} ($p>0.3$). Thus, our TEX_{86} values are likely not biased by terrestrial input. Both Methane Index (MI) and GDGT-2/Cren ratios show normal marine values (<0.20 and <0.12, respectively), so there is no indication for high abundance of methanotrophic archaea relative to Thaumarchaeota[33,34]. Furthermore, GDGT-0/Cren is low (<0.31), so there are no indications for enhanced contributions of methanogenic archaea to the pool of isoprenoid GDGTs used in TEX_{86}[(35)]. Finally, GDGT-2/GDGT-3 ratios are <4.5, ruling out significant impact of deep water production of GDGTs[36]. Together, these ratios indicate that GDGT distributions were likely not significantly affected by either GDGT-producing soil bacteria, methanotrophic or methanogenic archaea, or deep-dwelling Thaumarchaeota, thereby designating upper water column Thaumarchaeota as the main source and favouring the interpretation of TEX_{86}^{H} as a

444 SST proxy[37]. Another recently described ratio focuses on the different GDGT
445 distribution as produced by modern Thaumarchaeota in the Red Sea[5]. Based on core-
446 top datasets, fractional abundances of Red Sea GDGTs are known to differ from other
447 oceanic settings, notably in containing relatively more crenarchaeol regio-isomer
448 (Cren')[38]. This causes a different relationship between TEX_{86} and SST. Inglis *et al.*[5]
449 proposed the $\%GDGT_{RS}$ (Cren'/(GDGT-0+Cren')*100%) as a means of evaluating
450 whether a "Red Sea-type" GDGT distribution was present in the geological record. In
451 our tropical Eocene record, TEX_{86} is strongly driven by fractional abundance of
452 Cren', therefore there is also a strong correlation between TEX_{86} and $\%GDGT_{RS}$.
453 However, as Inglis *et al.* already noted, the particular Red Sea GDGT distribution
454 cannot be distinguished from a high temperature (>30ºC) distribution, so $\%GDGT_{RS}$
455 does not provide a way to disentangle the effects of high temperature versus Red Sea-
456 type GDGT distribution at this site. However we note that the several reasons that
457 have been proposed to account for the aberrant Red Sea GDGT distribution are not
458 likely to have played a role at Site 959. There is no environmental similarity between
459 Eocene Site 959 and the modern Red Sea that could account for a similarly adapted
460 population of endemic Thaumarchaeota, as the setting is not comparable
461 oceanographically or geomorphologically. Furthermore, our dinocyst record shows no
462 indication of high salinity or strong stratification throughout the record. Based on this,
463 we conclude that there is no reason to assume a similar TEX_{86} to SST relationship
464 between Site 959 and the modern Red Sea. Finally, we note that our new equatorial
465 record shows late Palaeocene TEX_{86}^{H} SST estimates of 31–33ºC, identical to time-
466 equivalent SSTs derived from glassy-preserved *Morozovella acuta* $\delta^{18}O$ and Mg/Ca
467 ratios and TEX_{86}^{H} from nearby sections in Nigeria[20], confirming accurate proxy
468 estimated SSTs at the study site.

469

470 **TEX_{86} calibrations**

471 *Calibrations*

472 Different calibrations have been proposed to translate TEX_{86} into SST. Of note is also
473 a recent paper by Ho and Laepple[39], who propose that the sedimentary GDGTs derive
474 from the deep-ocean and TEX_{86} therefore reflects deep (>500m) subsurface
475 temperatures rather than SST. However, their conclusions are controversial, as the
476 assumptions are inconsistent with all modern ocean and microbiological evidence,
477 and the statistical method is questionable[40]. Within the TEX_{86}-to-SST calibrations, a
478 first division can be made between calibrations based on core-top samples and those
479 based on mesocosm experiments. Here, we focus on applying different calibrations
480 based on core-top datasets[18,41], as these implicitly include ecological, water column
481 and diagenetic effects that are not incorporated in mesocosm experiments. Several
482 linear and non-linear core-top calibrations have been developed. Of these, the global
483 non-linear (logarithmic) TEX_{86}^{H} calibration of Kim *et al.*[18] and the spatially-varying
484 linear Bayesian TEX_{86} (BAYSPAR) calibration of Tierney and Tingley[19,41] are
485 particularly applicable and most commonly chosen for higher temperature settings
486 such as the Eocene. By treating TEX_{86} as the dependent variable, BAYSPAR is the
487 only calibration that does not suffer from regression dilution bias. For these
488 calibrations, the differences in absolute temperature and relative temperature change
489 in studies reporting TEX_{86} values between 0.5 and 0.75 are mostly within the error of
490 the proxy[18,19,41]. Significant differences only appear with TEX_{86} values above those
491 occurring in modern oceans (i.e. TEX_{86}>0.73) for which the TEX_{86} to SST calibration
492 has to be extrapolated. This is illustrated in **Extended Data Figure 2A**, which shows
493 that SST estimates based on the TEX_{86}^{H} and BAYSPAR calibration for Site 959 are

494 within error between TEX_{86} values of 0.67 and 0.80. However, the difference between
495 the calibrations increases at higher TEX_{86} values. For assessing temperature change in
496 a high temperature setting such as the equatorial Eocene, the choice of calibration
497 therefore becomes an important factor.
498
499 *Biophysical considerations*
500 For the modern ocean, a linear calibration results in a better statistical correspondence
501 between TEX_{86} and SST in the temperature range of 5ºC to 30ºC[18,42]. However, the
502 question remains if a linear calibration is the best choice for much warmer Eocene
503 oceans considering the biochemical mechanism underlying the TEX_{86}-SST
504 relationship. Hyperthermophilic archaea in culture synthesize an increasing
505 proportion of GDGTs with an increasing number of cyclopentane moieties with
506 increasing temperature[43–45], most likely as a homeoviscous adaptation of the cell
507 membrane[46]. However, the GDGTs included in the TEX_{86} ratio (GDGT1-3 and the
508 crenarchaeol isomer; **equation 1** below) constitute a minor part of the membrane
509 lipids of Thaumarchaeota. The dominant GDGTs are GDGT-0 and crenarchaeol[47–49].
510 Indeed, in the global core top data set, higher crenarchaeol and lower GDGT-0 are
511 recorded with higher temperatures, although their response is less strong than that of
512 the GDGT isomers included in TEX_{86} (fig. 4 in Kim *et al.*[18]). Thus, TEX_{86} does not
513 capture the full membrane adaptation of Thaumarchaeota to changing temperatures.
514 Interestingly, the ratio of crenarchaeol/GDGT-0 versus TEX_{86} shows a strongly non-
515 linear relationship in the global core top data (**Extended Data Figure 2C**). This trend
516 is similar to that observed between the TEX_{86} and the ring index (**Extended Data**
517 **Figure 2D**), which is the average number of cyclopentane rings of GDGTs 0-3,

crenarchaeol and its regio-isomer (**equation 2** below), and which also shows a strong relationship to temperature[50].

$$\mathrm{TEX}_{86} = \frac{[\mathrm{GDGT}-2] + [\mathrm{GDGT}-3] + [\mathrm{Cren}']}{[\mathrm{GDGT}-1] + [\mathrm{GDGT}-2] + [\mathrm{GDGT}-3] + [\mathrm{Cren}']} \quad (\mathbf{1})$$

$$\mathrm{RI} = 0 \times [\mathrm{GDGT}-0] + 1 \times [\mathrm{GDGT}-1] + 2 \times [\mathrm{GDGT}-2] + 3 \times [\mathrm{GDGT}-3] \quad (\mathbf{2}) \quad + 3 \times [\mathrm{GDGT}-3] + 4 \times [\mathrm{Cren}+\mathrm{Cren}']$$

In **ED Fig. 2C** and **2D**, both in terms of TEX_{86} versus ring index, and TEX_{86} versus Cren/GDGT-0, the Eocene data from Site 959 overlap the core top dataset, on both Red Sea and tropical latitude core-top data. This non-linear relationship indicates that at high temperatures, the TEX_{86} shows a relatively small response to temperature change relative to the amount of crenarchaeol versus GDGT-0 and the ring index. This suggests that with increasing temperatures, adaptation of the Thaumarchaeotal membrane is increasingly regulated through crenarchaeol and GDGT-0 rather than the GDGTs included in TEX_{86}. This should lead to a flattening of the slope between SST and TEX_{86} and therefore provides support for a logarithmic relationship. Additional support for this hypothesis comes from recent culturing experiments on three different Thaumarchaeota strains[49]. These show that for two strains, *Nitrosopumilus maritimus* and strain NAOA6, both the TEX_{86} and ring index (mainly driven by GDGT-0 and crenarchaeol) correlate with incubation temperature. However, in the third strain (NAOA2), the ring index but not TEX_{86} changes with growth temperature. This third strain had the highest growth temperature optimum and the strongest change in ring index from 28ºC to 35ºC. This suggests that, at temperatures >28ºC, membrane

adaptation to temperature in certain (high temperature) Thaumarchaeota may not be well reflected in the TEX_{86} ratio. It should be noted that a non-linear response was not found in mesocosm experiments at temperatures of up to 40ºC[51]. However, this calibration is substantially different from that of the global core top calibrations due to the unusually low amounts of the crenarchaeol regio-isomer[52]. A similarly low abundance of the crenarchaeol regio-isomer was noted for *Nitrosopumilus maritimus* and strain NAOA6[49]. In strain NAOA2[49] abundances of crenarchaeol regio-isomer were higher and did increase with temperature, suggesting it may be a better representation for high temperature-adapted marine Thaumarchaeota. Based on the above lines of biophysical evidence we argue that the slope of the TEX_{86} to temperature is likely to flatten at temperatures above the surface sediment dataset, such as the TEX_{86} values recorded in the Eocene of Site 959.

Implications

The use of the non-linear TEX_{86}^{H} calibration results in somewhat lower temperature estimates compared to the linear BAYSPAR calibration (**Extended Data Figure 2B**) for Site 959 in the early Eocene and late Palaeocene. Notably, for the Palaeocene, such estimates agree better with SSTs derived from glassy-preserved planktonic foraminiferal $\delta^{18}O$ and Mg/Ca records from nearby sections in Nigeria[20]. Additionally, the Site 959 TEX_{86}^{H} estimates fit well with the other SST constraints we use in our tropical Eocene compilation (**Extended Data Figure 5**). Finally, similarly reduced sensitivity of TEX_{86} (i.e. non-linearity) at the low end of the temperature range is undisputed as it is apparent in both mesocosm experiments[52], but also in the global core-top dataset[18,53]. We therefore apply the TEX_{86}^{H} calibration in our main analysis presented in the main manuscript. Nevertheless, the absolute temperature

567 estimates and magnitude of change obtained from the extrapolated part of the TEX_{86}
568 calibration curve should always be interpreted with care. For completeness, we also
569 present the results for the meridional temperature gradient and polar amplification
570 analysis using BAYSPAR in **Extended Data Figure 3**. This confirms that the use of
571 TEX_{86}^{H} rather than BAYSPAR implies a conservative estimate of middle-late Eocene
572 cooling and MECO warming at Site 959 and thus a low estimate of (early Eocene)
573 meridional temperature gradients and a maximum estimate of polar amplification
574 compared to BAYSPAR. Crucially, however, the choice of calibration does not affect
575 the trends in tropical surface temperatures (**Extended Data Figure 3A**), or the fact
576 that they parallel deep-ocean temperatures – and therefore does not affect our
577 conclusion regarding the drivers of Eocene climate change. The larger Eocene range
578 of tropical temperatures reconstructed using BAYSPAR does imply that sea surface
579 temperatures at Site 959 varied more than deep sea temperatures during the Eocene,
580 suggesting tropical rather than polar amplification. Regardless, the relation between
581 tropical and deep sea temperatures remains linear, reflecting a constant polar
582 amplification factor (**Extended Data Figure 3C)**.
583
584 **Age model Site 959**
585 Eocene sediments from Site 959 were too weakly magnetized to yield reliable
586 palaeomagnetic results[16]. Our age model is therefore based on a combination of bio-
587 and chemostratigraphy and supported by cyclic variations in sediment coloration
588 (**Extended Data Figure 1**). Although the dinoflagellate cyst assemblages support an
589 Eocene age of the analysed material, they did not yield many biostratigraphic events
590 with a well-calibrated age in the tropics[54]. A total number of 76 additional standard
591 smear slides (**Supplementary Data**) were analysed for calcareous nannofossil and

allowed for improvement of the initial biostratigraphic framework[55]. Biochronological estimates from the low latitude nannofossil biozonation[56] were converted to the Geologic Time Scale 2012 (GTS2012)[57] using the relative position of each biohorizon within the respective magnetochron. In total, 10 robust nannofossil tie-points were used (**Extended Data Table 1**). The Base and Top of *Chiasmolithus gigas* could not be used at this site due to extremely low abundance of this species. Therefore, alternative biohorizons among the evolutionary lineage *Sphenolithus furcatolithoides* morph. A – *Sphenolithus cuniculus – S. furcatolithoides* morph. B were used. Based on the co-occurrence of two non-synchronous bio-events (Base *Nannotetrina alata* gr. and Base *Nannotetrina cristata*) at the same depth (between 740.95 and 741.63 mbsf) and supported by a sudden shift in the nannofossil assemblage, the presence of a hiatus was inferred in Core 35R at ~741 mbsf. The presence of *Nannotetrina alata sensu strico* in combination with *Sphenolithus perpendicularis* and transitional forms of sphenoliths in at 740.95 mbsf suggests that the sediments just above the hiatus are very close in age to the actual base of *N. alata* group. Therefore, we also include this biohorizon in our age model. The lower boundary of the hiatus is based on linear extrapolation of the underlying sedimentation rate of 1.27 cm kyr^{-1}. This approach results in a hiatus of 1.5 Myr (48.0–46.5 Ma). To further constrain the age model, several chemostratigraphic tie-points were used. The onset of the carbon isotope excursion marking the Palaeocene-Eocene Thermal Maximum (~56 Ma) was recently identified at 804.09 mbsf[21]. In addition, the previously identified late Eocene minimum in osmium isotope ratios[58] ($^{187}Os/^{188}Os$) at 458.65 mbsf has an age of 34.4 Ma in the GTS2012 based on correlation to the Os isotope record at well-dated ODP Site 1218 and 1219[(59)]. These age constraints indicate that our data spans the entire Eocene. The age model is further supported by calculated sedimentation rates from

selected intervals, where high-resolution colour logs showed >4 easily distinguishable cycles. Sedimentation rates were calculated by assuming that these smallest-scale alternations are precession-forced, and were thus assigned a duration of 21 kyr per cycle. These sedimentation rates (blue lines in **Extended Data Figure 1**) correspond closely to those based on chemostratigraphy and biostratigraphy. Our age model implies that the warming interval 590–565 mbsf reflects the Middle Eocene Climatic Optimum (MECO), which is further supported by a shift in osmium isotope ratios that was also identified within the MECO at Sites 1263 and U1333 (RvdP, D. Selby, MJC, Y. Li, SMB, J. J. Middelburg, AS. Middle Eocene greenhouse warming facilitated by diminished weathering feedback. *Nat. Comm.* In Review). Due to a lack of nannofossils in the poorly recovered upper part of Hole 959D, linear extrapolation was used for the data points <466 mbsf. This places the Eocene-Oligocene boundary at 447.5 mbsf, which is in good agreement with the placing of the Oi1 glacial event based on the osmium isotope recovery after the 34.4 Ma minimum by Ravizza and Paquay[58].

Age models other sites

ODP Site 1172

The TEX_{86}-based SST record from Site 1172[3,60,61] was plotted (**Figure 2**) on an age model based on the magnetostratigraphy of Bijl *et al.*[62], in turn largely grounded on the original interpretation by Fuller and Touchard[63]. This was supplemented with three well-calibrated dinocyst events from Dallanave *et al.*[64] (top and bottom range *Charlesdowniea edwardsii*, and top range *Wilsonidium ornatum*) instead of the uncertain magnetochron reversals for this interval (552-578 mbsf).

Dahomey Basin, Nigeria

For the Sagamu Quarry and IB10B Core, Nigeria, published biostratigraphic and chemostratigraphic age constraints[20] were used. Specifically, Bot *Morozovella subbotinae*, Bot *Acarinina soldadoensis* were used for SQ and Bot *Acarinina soldadoensis*, Top *Morozovella acuta*, CIE onset and top CIE recovery were used for IB10B as age-depth tie-points.

Tropical sea surface temperature compilation

For the presented compilation, we integrate the new ODP Site 959 TEX_{86}-based SST record with several existing SST proxy records, specifically $\delta^{18}O$ of photosymbiont-bearing planktonic foraminifera *Morozovella* spp. (upper mixed layer) and *Acarinina* spp. (mixed layer) from the Sagamu Quarry (SQ), Nigeria[20] and Tanzania Drilling Project (TDP) sections[4,65], and near-surface dwelling *Turborotalia ampliapertura* from TDP[66]; Mg/Ca of *Morozovella* spp. from ODP Site 865[(67)] and SQ[20], *Acarinina* spp. from SQ[20], and *T. ampliapertura* from TDP[68]; TEX_{86} from ODP Site 925[(24,69)], 929[(5,24)], TDP[4], SQ and the IB10B Core, Nigeria[20]; and clumped isotope (Δ_{47}) thermometry of shallow-dwelling large benthic foraminifera from Evans *et al.*[6] (**Supplementary data**). We did not include data from South Dover Bridge[5] and Walvis Ridge[70], because plate tectonic reconstructions place them outside of the 30°–30° latitude band. Age models for all sites were converted to GTS2012 using published age-depth tie-points. For the Mg/Ca proxy, (normalised) Mg/Ca compositions were converted to SST using the Anand *et al.*[71] calibration, using the Eocene seawater Mg/Ca reconstruction from Evans *et al*.[6] and using H=0.42[(72)] to correct for power law dependence of test Mg/Ca on changing seawater Mg/Ca[(73)]. $\delta^{18}O$ to temperature conversion was done following Erez and Luz[74], assuming a

667 constant ice-free global $\delta^{18}O_{sw}$ of -1.2‰ VPDB[75] and (constant) latitudinal
668 corrections for TDP and SQ of 0.83‰ and 0.61‰, respectively[76]. A +2ºC correction
669 to convert reconstructed *T. ampliapertura* temperatures to SST, as used in the original
670 publication[68], was omitted here. It should be noted that different seawater chemistry
671 assumptions for the $\delta^{18}O$ and Mg/Ca proxies may result in shifts in reconstructed
672 temperatures, but do not qualitatively change trends or the correspondence between
673 trends. Multiple measured specimens per sample in the original studies have been
674 averaged into one value for this compilation. For the TEX_{86}-based records, samples
675 with aberrant GDGT ratios were removed following Inglis *et al.*[5]. The logarithmic
676 Kim *et al.*[18] TEX_{86}^{H} calibration was used in the main text and a full supplemental
677 analysis is provided using the linear BAYSPAR[19] calibration. For the BAYSPAR
678 calibration, the default search tolerance (2 standard deviations of raw TEX_{86} dataset)
679 was used for Site 959, 925 and 929, which yields a representative set of low-latitude
680 calibration localities. The search tolerance was stretched to 0.15 TEX units for the
681 Dahomey basin and TDP records to not only sample the possibly anomalous modern
682 Red Sea[38] but to include a broad representative sample of low-latitude localities.
683
684 **Global deep-ocean temperature compilation**
685 We base our deep-ocean temperature compilation on the benthic isotope stack
686 previously compiled by Zachos *et al.*[2] and supplement this with several high-
687 resolution benthic isotope records, specifically from ODP Site 690[(77,78)], ODP Site
688 748[(22)], ODP Site 1218[(79)], ODP Site 1209[(80)], ODP Site 1258[(81)], ODP Site 1262[(82)],
689 and ODP Site 1263[(83)]. After the respective species-specific corrections for
690 disequilibrium vital effects[84] were applied, $\delta^{18}O$ to temperature conversion was done
691 following Erez and Luz[74], assuming a constant ice-free global $\delta^{18}O_{sw}$ of -1.2‰

692 VPDB[75]. Age models for all sites were converted to GTS2012 using published age-
693 depth tie-points.
694
695 **CO_2 compilation**
696 The compiled CO_2 record plotted in **Figure 2** derives from boron isotopes from
697 TDP[8,85], with 68% confidence intervals as reported in Foster *et al.*[86], and alkenones
698 from ODP Site 612[(87)] and 925[(69)].
699
700 **Meridional temperature gradients**
701 As an approximation for the pole-to-equator temperature difference or meridional
702 temperature gradient (MTG), we calculate the difference between tropical mean SST
703 and deep-ocean temperatures. The latter are better constrained than high latitude SSTs
704 and exclude potential summer temperature biases that might plague available high
705 latitude SST records. We use deep-ocean temperatures based on $\delta^{18}O$, as these are
706 better constrained than those based on Mg/Ca, particularly because of the large
707 uncertainties regarding seawater Mg/Ca values as well as larger uncertainty between
708 different calibrations and corrections used to convert Mg/Ca to temperature. We note
709 that our approach of using the LOESS-fitted data provides robust estimates of long-
710 term changes in MTG, but is less appropriate for considering transient events, as fitted
711 event MTGs, e.g. for the PETM and MECO, are very dependent on the bandwidth of
712 the fit and the specific records used (**Extended Data Figure 8**).
713
714 **Sensitivity to late Eocene ice volume**
715 The Cenozoic benthic foraminiferal $\delta^{18}O$ signal reflects both deep-water temperature
716 and global ice volume changes. Although it is unlikely that large Antarctic ice sheets

were present in the warmest interval of the Cenozoic during the early Eocene, the extent of middle–late Eocene Antarctic glaciation is more uncertain (for discussion see e.g. Miller *et al.*[88], Barker *et al.*[89] and Gasson *et al.*[90]). Recent work argues for possible early–middle Eocene glaciation[91] but the dating of these sediments is highly uncertain. Although there might be evidence for glacial activity, the interpreted presence of early-middle Eocene large East Antarctic ice sheets is highly controversial, certainly in light of very warm temperatures on the East Antarctic margin[92]. Nevertheless, initial small ice caps in the middle-late Eocene would have had relatively enriched isotopic compositions of -20‰ to -35‰ VSMOW[93] relative to mean modern Antarctic ice of -54‰ VSMOW. We assess the effect of a range of middle-late Eocene ice volumes with different isotopic compositions on the mean $\delta^{18}O$ of Eocene seawater (**Extended Data Figure 6D**). This demonstrates that the effect of ice volume was likely not more than ~0.25‰, or ~1ºC in the latest Eocene. To further illustrate this, we present both the record of ice-free deep-ocean temperature evolution and a second line based on a linear build-up of late Eocene ice volume from 39.5 Ma (post-MECO) onwards to a latest Eocene (34.0 Ma) maximum of $10 * 10^6$ km^3[94,95] with an isotopic composition of -25‰ VSMOW[93] (**Extended Data Figure 6A).** This makes a maximum difference of about 0.8ºC ($\Delta\delta^{18}O_{sw}$ of 0.18‰) in the latest Eocene. We further propagate this uncertainty into the analysis of meridional temperature gradients and polar amplification factors (**Extended Data Figure 6B-C**.)

CESM 1 model simulations

We performed fully-coupled general circulation model simulations using the NCAR Community Earth System Model version 1 (CESM 1)[96] applying a range of radiative

742 forcings equivalent to a range of CO_2 concentrations (560, 1120, 2240 and 4480 ppm;
743 simulations EO1–EO4, respectively). The simulations share the same generalised
744 Eocene palaeogeography to assess the effect of changing CO_2 by itself, and were all
745 run for greater than 3,000 years to equilibrium. Simulations using an earlier, and
746 generally similar version of this model were found to produce the best match to early
747 Eocene proxy temperatures within a multi-model ensemble[15] and preliminary
748 comparison reveals that these new simulations are slightly improved over the earlier
749 version for the early Eocene[20]. Results from the lower CO_2 simulations (560 and
750 1120) and further information on the model can be found in Goldner *et al.*[26]. This
751 version of CESM has a modern "fast" climate sensitivity of 2.9ºC for one pCO_2
752 doubling[96], and a nearly constant emergent "slow" climate sensitivity, or ESS, of
753 3.5ºC per doubling in the Eocene simulations used here. For comparison with the
754 proxies in this study, the four simulations with varying CO_2 were assigned specific
755 ages by matching the simulated deep-ocean temperatures to the proxy-based deep-
756 ocean temperature reconstruction curve. We then compare the resulting sea surface
757 temperatures at the same localities as the main sites in our proxy compilation (ODP
758 Site 865, 925/929, 959 and TDP) and surface-to-deep gradients to evaluate model
759 performance (**Supplementary Data**). Temperature at the proxy data localities was
760 sampled in a 4° radius. This approach avoids the circularity of adjusting the climate
761 model radiative forcing to match surface temperature records, and also provides a
762 target that circumvents the uncertainty introduced by the various errors and
763 uncertainties in surface temperature records. In these simulations, bottom water
764 temperatures in the 4480 ppm scenario (simulation EO4) are representative of a hot
765 Early Eocene Climatic Optimum extreme (deep-ocean 13–14ºC, following the
766 conventions of Huber and Caballero[14]) whereas the 560 ppm scenario (simulation

767 EO1) is comparable to the latest Eocene (deep-ocean 4–5ºC), with intermediate
768 simulations (EO2 and EO3) in between and comparable to the middle Eocene.
769
770 **Polar amplification factor calculations**
771 First, to gain an estimate of the factor by which polar temperature change is amplified
772 relative to the tropics (*i.e.* the polar amplification factor), we performed a Deming
773 regression, accounting for error in both variables, of the Site 959 record against the
774 deep sea stack of temperatures, with data binned into 1-Myr bins from 34–58 Ma. We
775 did not include data from the EOT and earliest Oligocene, to exclude major effects of
776 ice volume changes on seawater $\delta^{18}O$. To assess the robustness of the single
777 regression, we followed a probabilistic approach using Monte Carlo resampling with
778 full propagation of errors. First, we generated 1000 iterations of both the tropical SST
779 and deep-ocean temperature datasets. In these iterations, each data point is resampled
780 within the 95% confidence limits of its propagated analytical plus calibration
781 uncertainty, assuming Gaussian distribution of errors. Using these, we calculated
782 1000 iterations of a Deming regression of DWT against tropical SST, with data
783 binned into 1-Myr bins from 34–58 Ma and propagated errors related to binning used
784 in the regression. We plotted the resulting suite of 1000 slopes as a probability density
785 function of the polar amplification factor. This exercise was performed using the full
786 tropical temperature compilation and the single Site 959 record. We additionally
787 performed a Deming regression of the Site 959 record against the high latitude Site
788 1172 record as a supplementary analysis. The latter analysis generates a similar polar
789 amplification factor, but with larger scatter and uncertainty. This is due to the smaller
790 amount of data points in the Site 1172 SST record relative to the benthic $\delta^{18}O$ stack,

and differences in the detailed pattern of Eocene cooling between Site 1172 compared to Site 959 and the deep-ocean temperature record.

Earth System Sensitivity calculations

To provide estimates of Eocene ESS *sensu* Lunt et al.[97], we combined our proxy and model reconstructions of temperature with the few available CO_2 reconstructions based on boron isotopes[8], involving 1 sample for the early (54–49 Ma), 2 samples for the middle (48–42 Ma), and 1 sample for the late Eocene (38–35 Ma). We derived temperatures by sampling the proxy compilation within the designated age brackets. We use tropical and deep-ocean temperature change (dT) as minimum and maximum estimates of dT. Between these, a uniform "flat" probability distribution is assumed. We convert changes in boron-based CO_2 estimates to radiative forcing in W m^{-2} using the radiative forcing fit from Byrne and Goldblatt[98]. With the above approach, we derived estimates of ESS in K W^{-1} m^{-2} for the early Eocene compared to the middle and late Eocene and to the pre-industrial. Uncertainties are based on propagated uncertainties of temperature change and radiative forcing derived by resampling these datasets 1000 times within their 95% confidence limits (propagated analytical plus calibration uncertainty for temperature, reported 95% confidence limits from the original work[8] for CO_2). In this, we removed radiative forcings <0, *i.e.* we assume there is no negative forcing associated with increasing CO_2. Given the good match between proxies and presented model simulations, we also calculated ESS using the model-derived global mean temperatures and CO_2 proxy data.

Data availability statement

The authors declare that the data supporting the findings of this study are available within the paper and its Supplementary Information files. Original raw data (palynology counts and GDGT concentrations and chromatograms) are available from the corresponding author upon request.

Code availability statement

The model used in this study is the NCAR CESM1 with CAM4 atmosphere, which is freely available from NCAR (http://www.cesm.ucar.edu/models/cesm1.0/).

825 **Methods references**

826 31. Hopmans, E. C., Schouten, S. & Sinninghe Damsté, J. S. The effect of
827 improved chromatography on GDGT-based palaeoproxies. *Org. Geochem.* **93,** 1–6
828 (2016).
829 32. Hopmans, E. C. *et al.* A novel proxy for terrestrial organic matter in sediments
830 based on branched and isoprenoid tetraether lipids. *Earth Planet. Sci. Lett.* **224,**
831 107–116 (2004).
832 33. Weijers, J. W. H., Lim, K. L. H., Aquilina, A., Sinninghe Damsté, J. S. &
833 Pancost, R. D. Biogeochemical controls on glycerol dialkyl glycerol tetraether lipid
834 distributions in sediments characterized by diffusive methane flux. *Geochem.*
835 *Geophys. Geosystems* **12,** Q10010 (2011).
836 34. Zhang, Y. G. *et al.* Methane Index: A tetraether archaeal lipid biomarker
837 indicator for detecting the instability of marine gas hydrates. *Earth Planet. Sci.*
838 *Lett.* **307,** 525–534 (2011).
839 35. Blaga, C. I., Reichart, G.-J., Heiri, O. & Damsté, J. S. S. Tetraether membrane
840 lipid distributions in water-column particulate matter and sediments: a study of 47
841 European lakes along a north–south transect. *J. Paleolimnol.* **41,** 523–540 (2009).
842 36. Taylor, K. W. R., Huber, M., Hollis, C. J., Hernandez-Sanchez, M. T. &
843 Pancost, R. D. Re-evaluating modern and Palaeogene GDGT distributions:
844 Implications for SST reconstructions. *Glob. Planet. Change* **108,** 158–174 (2013).
845 37. Schouten, S., Hopmans, E. C., Schefuß, E. & Sinninghe Damsté, J. S.
846 Distributional variations in marine crenarchaeotal membrane lipids: a new tool for
847 reconstructing ancient sea water temperatures? *Earth Planet. Sci. Lett.* **204,** 265–
848 274 (2002).

849 38. Trommer, G. *et al.* Distribution of Crenarchaeota tetraether membrane lipids
850 in surface sediments from the Red Sea. *Org. Geochem.* **40,** 724–731 (2009).
851 39. Ho, S. L. & Laepple, T. Flat meridional temperature gradient in the early
852 Eocene in the subsurface rather than surface ocean. *Nat. Geosci.* **9,** 606–610
853 (2016).
854 40. Tierney, J. E., Damsté, J. S. S., Pancost, R. D., Sluijs, A. & Zachos, J. C.
855 Eocene temperature gradients. *Nat. Geosci.* **10,** ngeo2997 (2017).
856 41. Tierney, J. E. & Tingley, M. P. A TEX86 surface sediment database and
857 extended Bayesian calibration. *Sci. Data* **2,** (2015).
858 42. Kim, J.-H., Schouten, S., Hopmans, E. C., Donner, B. & Sinninghe Damsté, J.
859 S. Global sediment core-top calibration of the TEX86 paleothermometer in the
860 ocean. *Geochim. Cosmochim. Acta* **72,** 1154–1173 (2008).
861 43. De Rosa, M., Gambacorta, A., Nicolaus, B. & Bu'Lock, J. D. Complex lipids
862 of Caldariella acidophila, a thermoacidophile archaebacterium. *Phytochemistry* **19,**
863 821–825 (1980).
864 44. Lai, D., Springstead, J. R. & Monbouquette, H. G. Effect of growth
865 temperature on ether lipid biochemistry in Archaeoglobus fulgidus. *Extremophiles*
866 **12,** 271–278 (2008).
867 45. Boyd, E. S. *et al.* Temperature and pH controls on glycerol dibiphytanyl
868 glycerol tetraether lipid composition in the hyperthermophilic crenarchaeon
869 Acidilobus sulfurireducens. *Extremophiles* **15,** 59–65 (2011).
870 46. Gliozzi, A., Paoli, G., De Rosa, M. & Gambacorta, A. Effect of isoprenoid
871 cyclization on the transition temperature of lipids in thermophilic archaebacteria.
872 *Biochim. Biophys. Acta BBA - Biomembr.* **735,** 234–242 (1983).

873 47. Schouten, S. *et al.* Intact Membrane Lipids of "Candidatus Nitrosopumilus
874 maritimus," a Cultivated Representative of the Cosmopolitan Mesophilic Group I
875 Crenarchaeota. *Appl. Environ. Microbiol.* **74,** 2433–2440 (2008).
876 48. Pitcher, A. *et al.* Core and Intact Polar Glycerol Dibiphytanyl Glycerol
877 Tetraether Lipids of Ammonia-Oxidizing Archaea Enriched from Marine and
878 Estuarine Sediments. *Appl. Environ. Microbiol.* **77,** 3468–3477 (2011).
879 49. Elling, F. J., Könneke, M., Mußmann, M., Greve, A. & Hinrichs, K.-U.
880 Influence of temperature, pH, and salinity on membrane lipid composition and
881 TEX86 of marine planktonic thaumarchaeal isolates. *Geochim. Cosmochim. Acta*
882 **171,** 238–255 (2015).
883 50. Zhang, Y. G., Pagani, M. & Wang, Z. Ring Index: A new strategy to evaluate
884 the integrity of TEX86 paleothermometry. *Paleoceanography* **31,** 220–232 (2016).
885 51. Schouten, S., Forster, A., Panoto, F. E. & Sinninghe Damsté, J. S. Towards
886 calibration of the TEX86 palaeothermometer for tropical sea surface temperatures
887 in ancient greenhouse worlds. *Org. Geochem.* **38,** 1537–1546 (2007).
888 52. Wuchter, C., Schouten, S., Coolen, M. J. L. & Sinninghe Damsté, J. S.
889 Temperature-dependent variation in the distribution of tetraether membrane lipids
890 of marine Crenarchaeota: Implications for TEX86 paleothermometry.
891 *Paleoceanography* **19,** PA4028 (2004).
892 53. Ho, S. L. *et al.* Appraisal of TEX86 and thermometries in subpolar and polar
893 regions. *Geochim. Cosmochim. Acta* **131,** 213–226 (2014).
894 54. Awad, W. K. & Oboh-Ikuenobe, F. E. Early Paleogene dinoflagellate cysts
895 from ODP Hole 959D, Côte d'Ivoire-Ghana Transform Margin, West Africa: New
896 species, biostratigraphy and paleoenvironmental implications. *J. Afr. Earth Sci.*
897 **123,** 123–144 (2016).

898 55. Shafik, S., Watkins, D. K. & Shin, I. C. Calcareous Nannofossil Paleogene
899 Biostratigraphy, Côte d'Ivoire-Ghana Marginal Ridge, Eastern Equatorial Atlantic.
900 *Proc Ocean Drill Program Sci Results* **159,** 413–431 (1998).
901 56. Agnini, C. *et al.* Biozonation and biochronology of Paleogene calcareous
902 nannofossils from low and middle latitudes. *Newsl. Stratigr.* **47,** 131–181 (2014).
903 57. Gradstein, F. M., Ogg, J. G., Schmitz, M. D. & Ogg, G. M. *The Geologic Time*
904 *Scale 2012*. (Elsevier Science Limited, 2012).
905 58. Ravizza, G. & Paquay, F. Os isotope chemostratigraphy applied to organic-
906 rich marine sediments from the Eocene-Oligocene transition on the West African
907 margin (ODP Site 959). *Paleoceanography* **23,** PA2204 (2008).
908 59. Dalai, T. K., Ravizza, G. E. & Peucker-Ehrenbrink, B. The Late Eocene
909 187Os / 188Os excursion: Chemostratigraphy, cosmic dust flux and the Early
910 Oligocene glaciation. *Earth Planet. Sci. Lett.* **241,** 477–492 (2006).
911 60. Bijl, P. K. *et al.* Transient Middle Eocene Atmospheric CO2 and Temperature
912 Variations. *Science* **330,** 819–821 (2010).
913 61. Sluijs, A. *et al.* Southern ocean warming, sea level and hydrological change
914 during the Paleocene-Eocene thermal maximum. *Clim Past* **7,** 47–61 (2011).
915 62. Bijl, P. K., Sluijs, A. & Brinkhuis, H. A magneto- and chemostratigraphically
916 calibrated dinoflagellate cyst zonation of the early Palaeogene South Pacific
917 Ocean. *Earth-Sci. Rev.* **124,** 1–31 (2013).
918 63. Fuller, M. & Touchard, Y. On the Magnetostratigraphy of the East Tasman
919 Plateau Timing of the Opening of the Tasmanian Gateway and Paleoenvironmental
920 Changes. in *The Cenozoic Southern Ocean: Tectonics, Sedimentation, and Climate*
921 *Change Between Australia and Antarctica* (eds. Exon, N. F., Kennett, J. P. &
922 J.lone, M.) 63–78 (American Geophysical Union, 2004). doi:10.1029/151GM05

923 64. Dallanave, E. *et al.* Constraining early to middle Eocene climate evolution of
924 the southwest Pacific and Southern Ocean. *Earth Planet. Sci. Lett.* **433,** 380–392
925 (2016).
926 65. Aze, T. *et al.* Extreme warming of tropical waters during the Paleocene–
927 Eocene Thermal Maximum. *Geology* **42,** 739–742 (2014).
928 66. Pearson, P. N. *et al.* Extinction and environmental change across the Eocene-
929 Oligocene boundary in Tanzania. *Geology* **36,** 179–182 (2008).
930 67. Tripati, A. K. *et al.* Tropical sea-surface temperature reconstruction for the
931 early Paleogene using Mg/Ca ratios of planktonic foraminifera. *Paleoceanography*
932 **18,** 1101 (2003).
933 68. Lear, C. H., Bailey, T. R., Pearson, P. N., Coxall, H. K. & Rosenthal, Y.
934 Cooling and ice growth across the Eocene-Oligocene transition. *Geology* **36,** 251–
935 254 (2008).
936 69. Zhang, Y. G., Pagani, M., Liu, Z., Bohaty, S. M. & DeConto, R. A 40-million-
937 year history of atmospheric CO2. *Phil Trans R Soc A* **371,** 20130096 (2013).
938 70. Boscolo Galazzo, F. *et al.* The middle Eocene climatic optimum (MECO): A
939 multiproxy record of paleoceanographic changes in the southeast Atlantic (ODP
940 Site 1263, Walvis Ridge). *Paleoceanography* **29,** 2014PA002670 (2014).
941 71. Anand, P., Elderfield, H. & Conte, M. H. Calibration of Mg/Ca thermometry
942 in planktonic foraminifera from a sediment trap time series. *Paleoceanography* **18,**
943 1050 (2003).
944 72. Hasiuk, F. J. & Lohmann, K. C. Application of calcite Mg partitioning
945 functions to the reconstruction of paleocean Mg/Ca. *Geochim. Cosmochim. Acta*
946 **74,** 6751–6763 (2010).

947 73. Evans, D. & Müller, W. Deep time foraminifera Mg/Ca paleothermometry:
948 Nonlinear correction for secular change in seawater Mg/Ca. *Paleoceanography* **27,**
949 PA4205 (2012).
950 74. Erez, J. & Luz, B. Experimental paleotemperature equation for planktonic
951 foraminifera. *Geochim. Cosmochim. Acta* **47,** 1025–1031 (1983).
952 75. Shackleton, N. J. & Kennett, J. P. Paleotemperature History of the Cenozoic
953 and the Initiation of Antarctic Glaciation: Oxygen and Carbon Isotope Analyses in
954 DSDP Sites 277, 279 and 281. *Initial Rep. Deep Sea Drill. Proj.* **29,** 743–755
955 (1975).
956 76. Zachos, J. C., Stott, L. D. & Lohmann, K. C. Evolution of Early Cenozoic
957 marine temperatures. *Paleoceanography* **9,** 353–387 (1994).
958 77. Kennett, J. P. & Stott, L. D. Abrupt deep-sea warming, palaeoceanographic
959 changes and benthic extinctions at the end of the Palaeocene. *Nature* **353,** 225–229
960 (1991).
961 78. Thomas, D. J., Zachos, J. C., Bralower, T. J., Thomas, E. & Bohaty, S.
962 Warming the fuel for the fire: Evidence for the thermal dissociation of methane
963 hydrate during the Paleocene-Eocene thermal maximum. *Geology* **30,** 1067–1070
964 (2002).
965 79. Coxall, H. K. & Wilson, P. A. Early Oligocene glaciation and productivity in
966 the eastern equatorial Pacific: Insights into global carbon cycling.
967 *Paleoceanography* **26,** PA2221 (2011).
968 80. Westerhold, T., Röhl, U., Donner, B., McCarren, H. K. & Zachos, J. C. A
969 complete high-resolution Paleocene benthic stable isotope record for the central
970 Pacific (ODP Site 1209). *Paleoceanography* **26,** PA2216 (2011).

971 81. Sexton, P. F. *et al.* Eocene global warming events driven by ventilation of
972 oceanic dissolved organic carbon. *Nature* **471,** 349–352 (2011).
973 82. Littler, K., Röhl, U., Westerhold, T. & Zachos, J. C. A high-resolution benthic
974 stable-isotope record for the South Atlantic: Implications for orbital-scale changes
975 in Late Paleocene–Early Eocene climate and carbon cycling. *Earth Planet. Sci.*
976 *Lett.* **401,** 18–30 (2014).
977 83. Lauretano, V., Hilgen, F. J., Zachos, J. C. & Lourens, L. J. Astronomically
978 tuned age model for the early Eocene carbon isotope events: A new high-resolution
979 δ13 Cbenthic record of ODP Site 1263 between ~ 49 and ~ 54 Ma. *Newsl. Stratigr.*
980 **49,** 383–400 (2016).
981 84. Shackleton, N. J. & Hall, M. A. The Late Miocene Stable Isotope Record, Site
982 926. *Proc Ocean Drill Program Sci Results* **154,** 367–373 (1997).
983 85. Pearson, P. N., Foster, G. L. & Wade, B. S. Atmospheric carbon dioxide
984 through the Eocene–Oligocene climate transition. *Nature* **461,** 1110–1113 (2009).
985 86. Foster, G. L., Royer, D. L. & Lunt, D. J. Future climate forcing potentially
986 without precedent in the last 420 million years. *Nat. Commun.* **8,** (2017).
987 87. Pagani, M., Zachos, J. C., Freeman, K. H., Tipple, B. & Bohaty, S. Marked
988 Decline in Atmospheric Carbon Dioxide Concentrations During the Paleogene.
989 *Science* **309,** 600–603 (2005).
990 88. Miller, K. G., Wright, J. D. & Browning, J. V. Visions of ice sheets in a
991 greenhouse world. *Mar. Geol.* **217,** 215–231 (2005).
992 89. Barker, P. F., Diekmann, B. & Escutia, C. Onset of Cenozoic Antarctic
993 glaciation. *Deep Sea Res. Part II Top. Stud. Oceanogr.* **54,** 2293–2307 (2007).

994 90. Gasson, E. *et al.* Exploring uncertainties in the relationship between
995 temperature, ice volume, and sea level over the past 50 million years. *Rev.*
996 *Geophys.* **50,** RG1005 (2012).
997 91. Gulick, S. P. S. *et al.* Initiation and long-term instability of the East Antarctic
998 Ice Sheet. *Nature* **552,** 225 (2017).
999 92. Pross, J. *et al.* Persistent near-tropical warmth on the Antarctic continent
1000 during the early Eocene epoch. *Nature* **488,** 73–77 (2012).
1001 93. DeConto, R. M. *et al.* Thresholds for Cenozoic bipolar glaciation. *Nature* **455,**
1002 652–656 (2008).
1003 94. Gasson, E. *et al.* Uncertainties in the modelled CO2 threshold for Antarctic
1004 glaciation. *Clim Past* **10,** 451–466 (2014).
1005 95. de Boer, B., Wal, R. S. W. van de, Bintanja, R., Lourens, L. J. & Tuenter, E.
1006 Cenozoic global ice-volume and temperature simulations with 1-D ice-sheet
1007 models forced by benthic δ18O records. *Ann. Glaciol.* **51,** 23–33 (2010).
1008 96. Shields, C. A. *et al.* The Low-Resolution CCSM4. *J. Clim.* **25,** 3993–4014
1009 (2012).
1010 97. Lunt, D. J. *et al.* Earth system sensitivity inferred from Pliocene modelling and
1011 data. *Nat. Geosci.* **3,** 60–64 (2010).
1012 98. Byrne, B. & Goldblatt, C. Radiative forcing at high concentrations of well-
1013 mixed greenhouse gases. *Geophys. Res. Lett.* **41,** 152–160 (2014).
1014

Extended Data Legends

Extended Data Figure 1 | Augmented age model of Hole 959D. Age-depth plot showing calcareous nannofossil and chemostratigraphic tie-points (diamonds with error bars plotted between minimum and maximum depth of tie-point) as presented in **Extended Data Table 1b**. Abbreviation mbsf stands for meters below seafloor; B, BC, and T stand for Base, Base Common and Top, respectively. Blue shaded regions represent depth-intervals for which sedimentation rates (blue lines) were calculated. Hiatus of ~1.5 Myr in Core 35 indicated as red curly line. Epochs and ages in million years ago (Ma) following GTS2012.

Extended Data Figure 2 | Comparison between different TEX_{86}-to-SST calibrations and different GDGT ratios. a, TEX_{86}-SST calibration lines (trendlines for BAYSPAR) for one logarithmic and several linear calibrations. Plotted symbols are the Hole 959D TEX_{86} record, to illustrate which part of the calibration is relevant for this study. Compared calibrations are: BAYSPAR[19,41] with default settings (search tolerance 2 TEX_{86} standard deviations; 0.13) (dark grey line, dark grey diamonds), BAYSPAR with increased search tolerance (0.2) (dashed line, light grey diamonds), Kim *et al.*[18] logarithmic TEX_{86}^{H} core-top calibration (red line, red diamonds), Kim *et al.* linear core-top calibration (light blue line) Kim *et al.* linear subset core-top calibration without Red Sea and polar ocean data (dark blue line). It is of note that the logarithmic TEX_{86}^{H} starts strongly diverging from the linear BAYSPAR and subset Kim *et al.* calibrations from TEX_{86} values of >0.8. **b**, Hole 959D SST record using different TEX_{86} calibrations. Same calibrations and line colours/types used as in panel a. **c**, Ratio of crenarchaeol divided by GDGT-0 against TEX_{86}, data from core-top

compilation[41] (black circles; Red Sea subset purple circles) and our Hole 959D record (red squares). **d**, Ring index *sensu* Zhang *et al.*[50] against TEX_{86}, data from core top compilation (black circles; Red Sea subset purple circles) and our Hole 959D record (red squares). The exponential regression line of Zhang *et al.* through the core top data is plotted as a black line.

Extended Data Figure 3 | Sensitivity of main results to TEX_{86} calibration. a, Above: tropical SST (ºC) compilation, proxy data as compiled in **Methods** (red symbols), with all TEX_{86}-based records converted to SST using the BAYSPAR calibration (default settings, search tolerance 2 standard deviations of the raw respective TEX_{86} datasets). Fitted LOESS model plotted as black line, 95% confidence interval as gray shading. Below: ice-free deep-ocean temperature (ºC) compilation, $\delta^{18}O$-based proxy data as compiled in **Methods**. Fitted LOESS model plotted as black line, 95% confidence interval as dark blue shading. **b,** Calculated meridional temperature gradient MTG (ºC) based on LOESS fits of proxy data (lines, propagated 95% confidence intervals as silhouettes). Black line with grey silhouette uses the tropical compilation with TEX_{86}^{H} calibration; blue line with blue silhouette uses the BAYSPAR calibration. **c,** Proxy (blue diamonds, tropical compilation; red diamonds, Site 959) deep-ocean temperature (ºC) against tropical sea surface temperature (ºC) using the BAYSPAR calibration for TEX_{86}-based records. Lines represent Deming regression analysis through proxy data (slope, or polar amplification factor 1.42 □ 0.14 (□ 1 SE) for tropical compilation; 0.75 □ 0.04 for Site 959). Proxy data grouped into 1-Myr bins from 34-58 Ma, with error bars representing standard deviation due to binning. This sensitivity analysis shows that calculated MTGs and the constant polar amplification factor are relatively robust to

1065 the specific TEX_{86} calibration used, although MTGs are somewhat less reduced in the
1066 early Eocene when using the BAYSPAR calibration. Polar amplification factors are
1067 lower, but reflect a linear relationship.
1068
1069 **Extended Data Figure 4 | Regression analysis between reconstructed SST and**
1070 **abundance of upwelling indicators. a**, TEX_{86}^{H}-based SST (ºC) (red diamonds, upper
1071 left vertical axis), Protoperidinioid abundance (% of total dinocyst assemblage)
1072 (brown dots, right vertical axis), and total organic carbon TOC (% of sediment) (black
1073 dots, lower left vertical axis) records of ODP Site 959. Dashed lines represent a hiatus
1074 in Site 959. Plotted against age in millions of years ago (Ma), Geological Time Scale
1075 2012. **b**, Regression analysis between SST and percentage of Protoperidinioid
1076 dinocysts of total dinocyst assemblage, showing a non-significant relationship with
1077 very low fit (brown line, 90% confidence interval as brown shading, $R^2 = 0.00$, $p =$
1078 0.75) and a better fit ($R^2 = 0.35$) that is significant ($p < 0.01$) when only the late
1079 Eocene (post-MECO) part of the record is considered (blue-grey line, 90% CI as blue-
1080 grey shading). **c**, Regression analysis between SST and percentage of total organic
1081 carbon in sediment, showing a significant negative correlation for the whole record
1082 ($R^2 = 0.39$, $p < 0.001$; dark grey line, 90% CI as dark grey shading) and the late
1083 Eocene subset ($R^2 = 0.37$, $p < 0.01$; blue-grey line, 90% CI as blue-grey shading).
1084
1085 **Extended Data Figure 5 | Eocene multi-proxy tropical SST compilation.**
1086 Compilation as presented in **Figure 2**, here plotted per site and proxy, with data
1087 sources in legend. *Moro*., *Aca*., and *Turbo*. abbreviations for foraminifera genera
1088 *Morozovella*, *Acarinina* and *Turborotalia*, respectively. The dashed line in the Site
1089 959 record represents a hiatus. Conservative estimates of propagated calibration and

analytical errors are ±2.6 ºC for TEX_{86}^{H}, ±1.6 ºC for $\delta^{18}O$, and ±1.3 ºC for Mg/Ca (± 1 sd). Δ_{47} uncertainties as reported in the original study[6], with minimum and maximum range. Uncertainties plotted on same relative vertical temperature scale as graph, to facilitate comparison. Plotted against age in millions of years ago (Ma), Geological Time Scale 2012, with age range of Epochs. Palaeocene and Oligocene abbreviated as "Pal." and "Olig.", respectively.

Extended Data Figure 6 | Sensitivity of main results to late Eocene ice volume. Above: tropical SST (ºC) compilation, proxy data as compiled in **Methods** (red symbols). Fitted LOESS model plotted as black line, 95% confidence interval as gray shading. Below: deep-ocean temperature (ºC) compilation, $\delta^{18}O$-based proxy data as compiled in **Methods**. Ice-free deep-ocean temperatures and fitted LOESS model as grey dots and line, respectively, and deep-ocean temperature compilation and fitted LOESS model including late Eocene ice volume effect (**Methods**) as blue dots and line. 95% LOESS confidence intervals as shading. **b,** Calculated meridional temperature gradient MTG (ºC) based on LOESS fits of proxy data (lines, propagated 95% confidence intervals as silhouettes). Black line with grey silhouette uses the ice-free deep-ocean temperatures; blue line with blue silhouette includes the late Eocene ice volume effect on deep-ocean temperature. **c,** Proxy (blue diamonds, tropical compilation; red diamonds, Site 959) deep-ocean temperature (ºC) including late Eocene ice volume effect against tropical sea surface temperature (ºC). Lines represent Deming regression analysis through proxy data (slope, or polar amplification factor 2.07 □ 0.25 (□ 1 SE) for tropical compilation; 1.19 □ 0.06 for Site 959). Proxy data grouped into 1-Myr bins from 34-58 Ma, with error bars representing standard deviation due to binning. **d,** sensitivity of $\delta^{18}O$ of Eocene

1115 seawater (‰ VSMOW) to buildup of 0–10^7 km^3 ice with varying isotopic
1116 composition.
1117
1118 **Extended Data Figure 7 | Linear relationship between high-latitude and tropical**
1119 **sea surface temperature.** Site 1172 TEX_{86}-based SST (record plotted in **Extended**
1120 **Data Figure 5**) against Site 959 TEX_{86}-based SST. Lines represent Deming
1121 regression analysis through proxy data (slope, or polar amplification factor 1.66
1122 0.57). Proxy data grouped into 1-Myr bins from 34-58 Ma, with error bars
1123 representing standard deviation due to binning. Peak PETM and peak MECO SSTs
1124 plotted as separate annotated points that fall within uncertainty of the regression line.
1125
1126 **Extended Data Figure 8 | PETM temperature gradient proxy-model comparison.**
1127 **a,** Above: tropical SST (ºC) compilation, proxy data as compiled in **Methods** (red
1128 symbols). Fitted LOESS model plotted as red line, 95% confidence interval as pink
1129 shading. Below: ice-free deep-ocean temperature (ºC) compilation, $\delta^{18}O$-based proxy
1130 data as compiled in **Methods**. GCV-optimized fitted LOESS model (as in **Figure 3**)
1131 plotted as gray line, 95% CI as gray shading. Alternative LOESS model with small
1132 bandwidth (0.25 * GCV-optimized span) that tracks deep-ocean PETM temperature
1133 more closely as blue line, 95% CI as blue shading. Plotted together with the PETM
1134 simulation of Kiehl and Shields[28] (black open squares, seasonal range error bars) with
1135 altered cloud parameters (CP_PETM). **b,** Calculated meridional temperature gradient
1136 MTG (ºC) based on LOESS fits of proxy data and of model simulation CP_PETM.
1137 Gray line uses GCV-optimized fitted LOESS model, blue line uses smaller bandwidth
1138 deep-ocean LOESS model (propagated 95% confidence intervals as shading). Note
1139 that the PETM MTG pattern is complex due to sensitivity to the specific records, age

models and filtering used, and might have evolved over the course of the event. Nevertheless, peak PETM MTG is well constrained and matches simulation CP_PETM poorly. Plotted against age in millions of years ago (Ma), Geological Time Scale 2012.

Extended Data Figure 9 | Probability distributions of Eocene Earth System Sensitivity. ESS estimates using proxy (**a**) and model (**b**) temperatures in combination with proxy-based CO_2, derived as in **Methods**. Eocene ESS separated into late Eocene relative to EECO (red), middle Eocene relative to EECO (purple) and middle Eocene relative to late Eocene (blue). ESS estimates of EECO relative to pre-industrial (black) have lower error due to high precision of pre-industrial CO_2 and temperature, but include additional long-term non-CO_2 effects.

Tables

Extended Data Table 1 | Palaeolatitude and age constraints of Site 959 over the Eocene. a, Palaeolatitudes reconstructed with GPlates using the hotspot reference frame of Matthews *et al.*[30] and the palaeomagnetic reference of Torsvik *et al.*[99]. Present latitude 3.6276˚N, longitude 2.7352˚W. **b,** Bio- and chemostratigraphic age-depth tiepoints used in developing the age model for the Eocene of Site 959. Abbreviation mbsf stands for meters below seafloor; B, BC, and T stand for Base range, Base Common range and Top range, respectively.

Extended Data references

99. Torsvik, T. H. *et al.* Phanerozoic polar wander, palaeogeography and dynamics. *Earth-Sci. Rev.* **114,** 325–368 (2012).

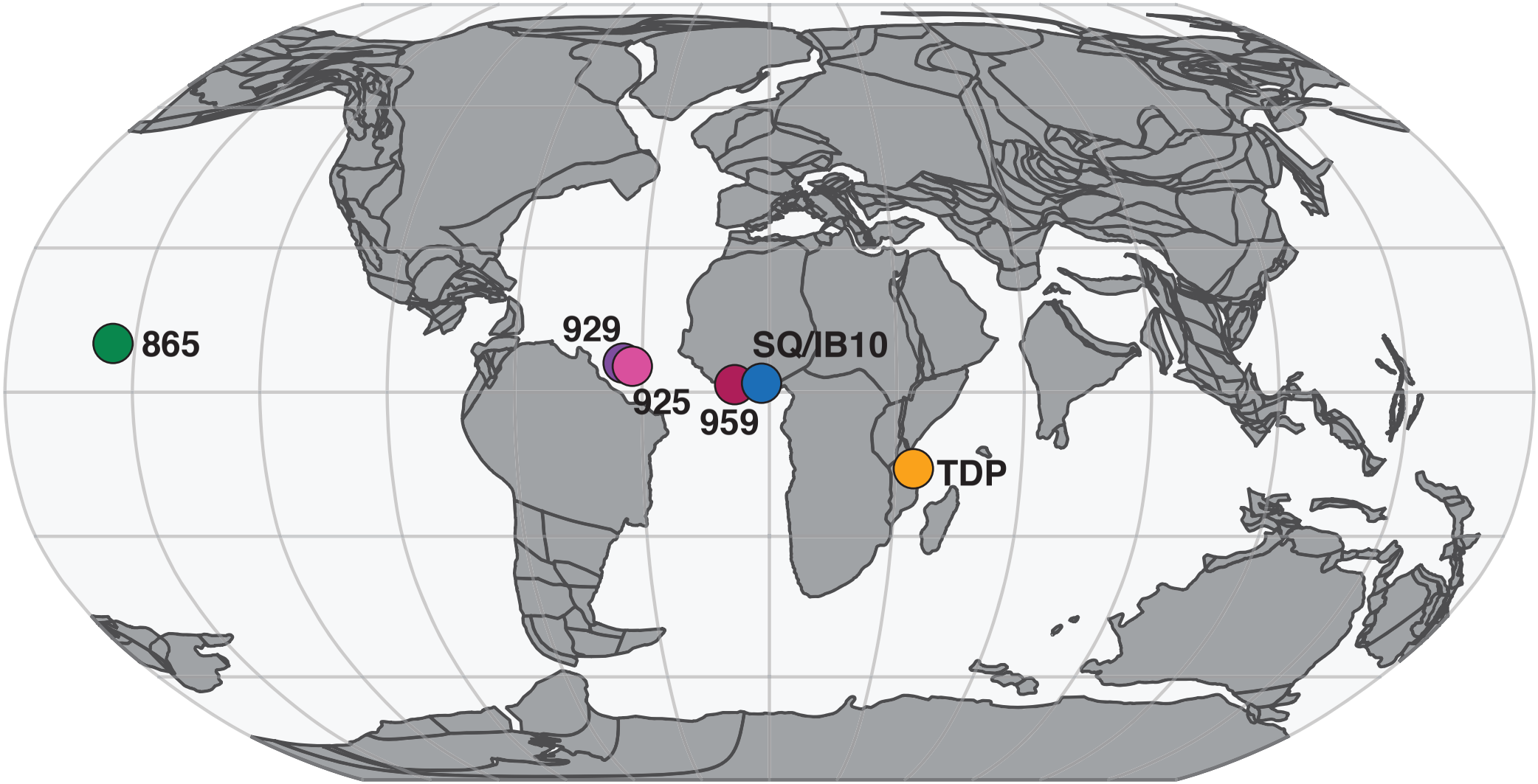
865
929
925
959
SQ/IB10
TDP

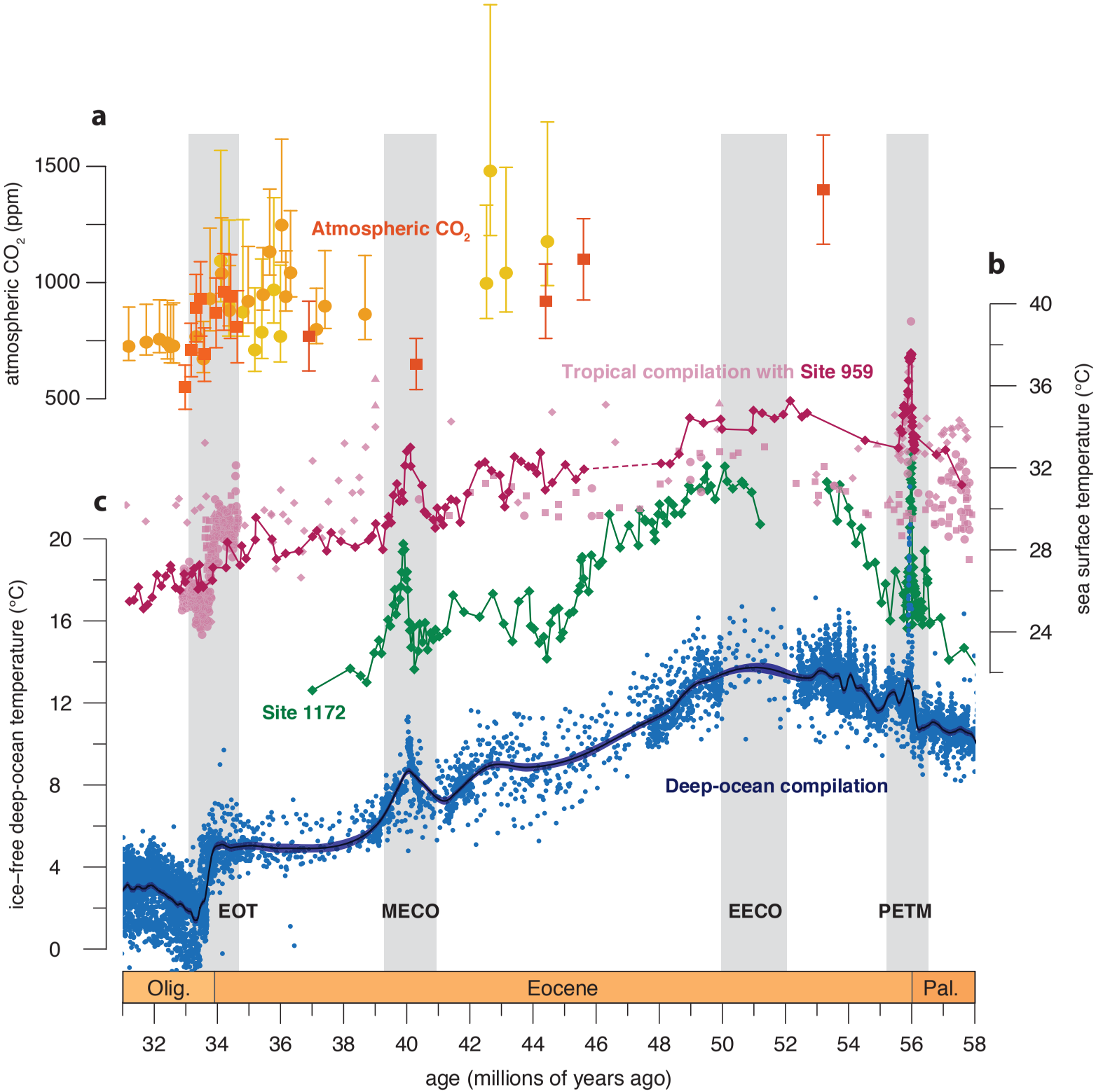
a
b
c
atmospheric CO2 (ppm)
1500
1000
500
Atmospheric CO2
Tropical compilation with Site 959
sea surface temperature (°C)
40
36
32
28
24
ice–free deep-ocean temperature (°C)
20
16
12
8
4
0
Site 1172
Deep-ocean compilation
EOT
MECO
EECO
PETM
Olig.
Eocene
Pal.
32
34
36
38
40
42
44
46
48
50
52
54
56
58
age (millions of years ago)

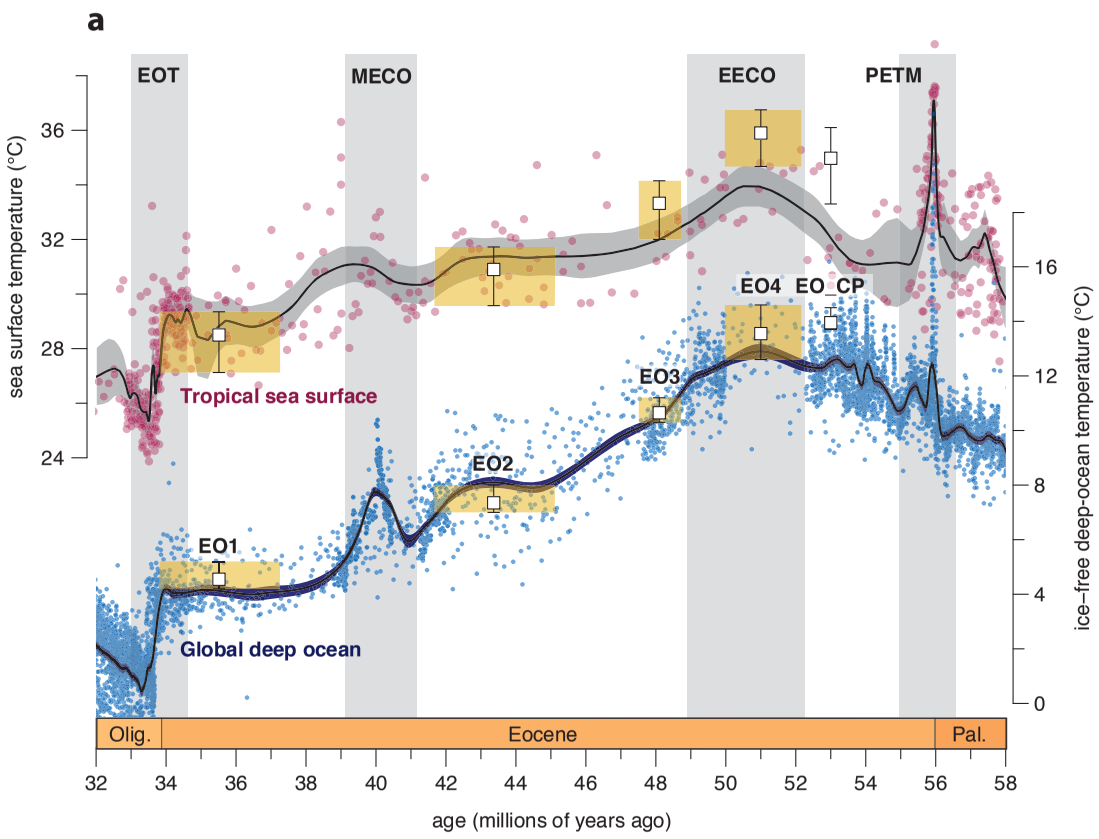
a
EOT
MECO
EECO
PETM
EO4
EO_CP
EO3
EO2
EO1
Tropical sea surface
Global deep ocean
sea surface temperature (°C)
ice–free deep-ocean temperature (°C)
Olig.
Eocene
Pal.
age (millions of years ago)

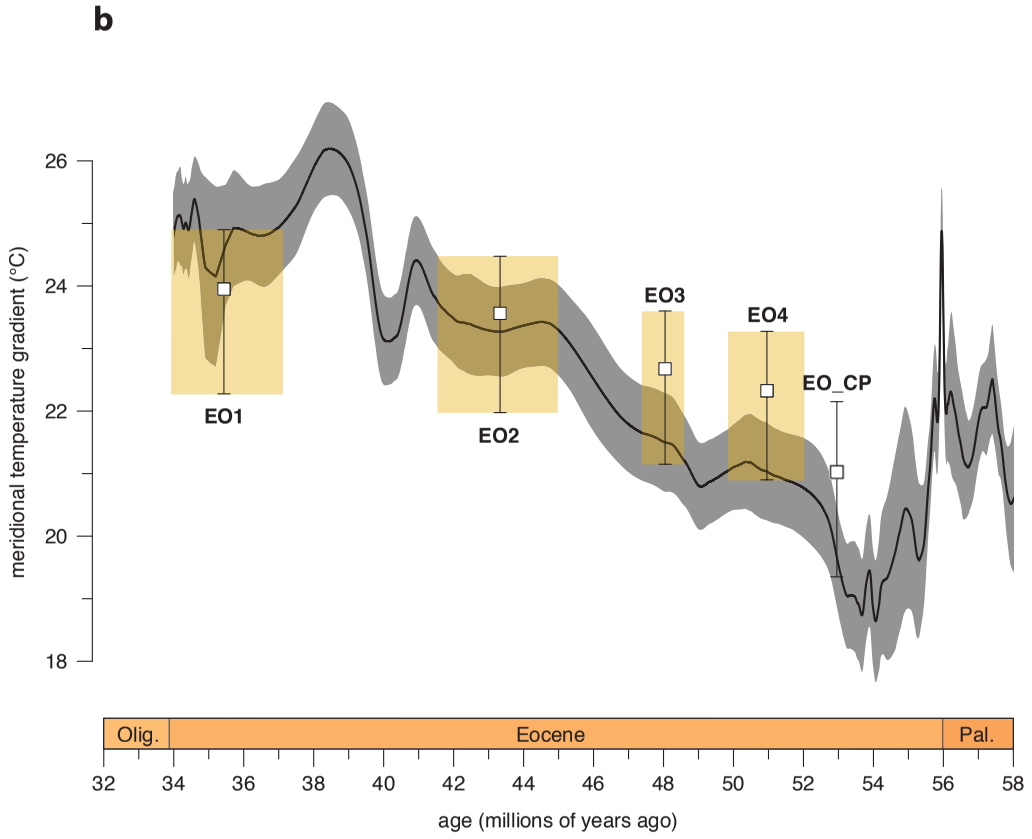
b
EO1
EO2
EO3
EO4
EO_CP
meridional temperature gradient (°C)
Olig.
Eocene
Pal.
age (millions of years ago)

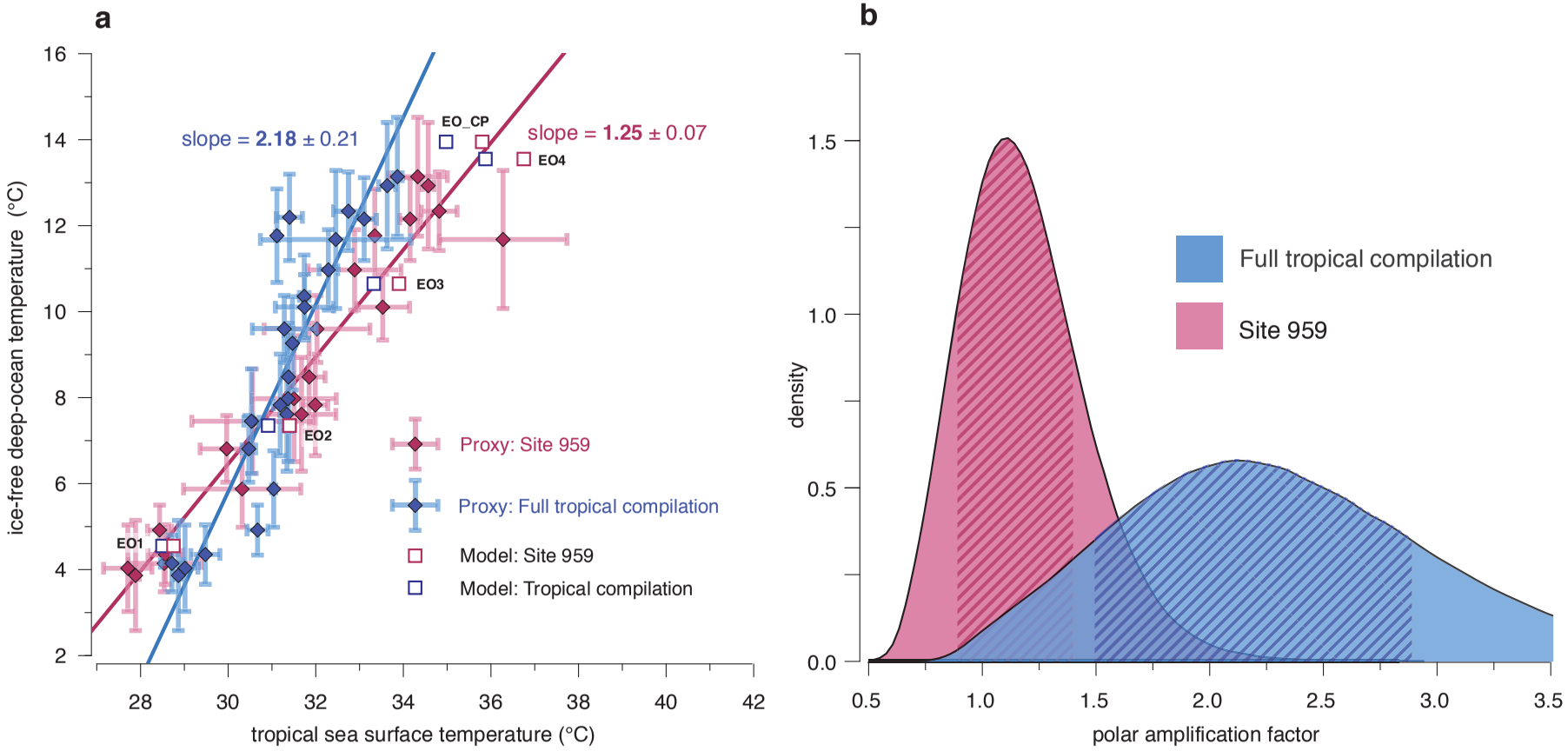
a
b
slope = 2.18 ± 0.21
slope = 1.25 ± 0.07
EO_CP
EO4
EO3
EO2
EO1
Proxy: Site 959
Proxy: Full tropical compilation
Model: Site 959
Model: Tropical compilation
ice-free deep-ocean temperature (°C)
tropical sea surface temperature (°C)
density
polar amplification factor
Full tropical compilation
Site 959

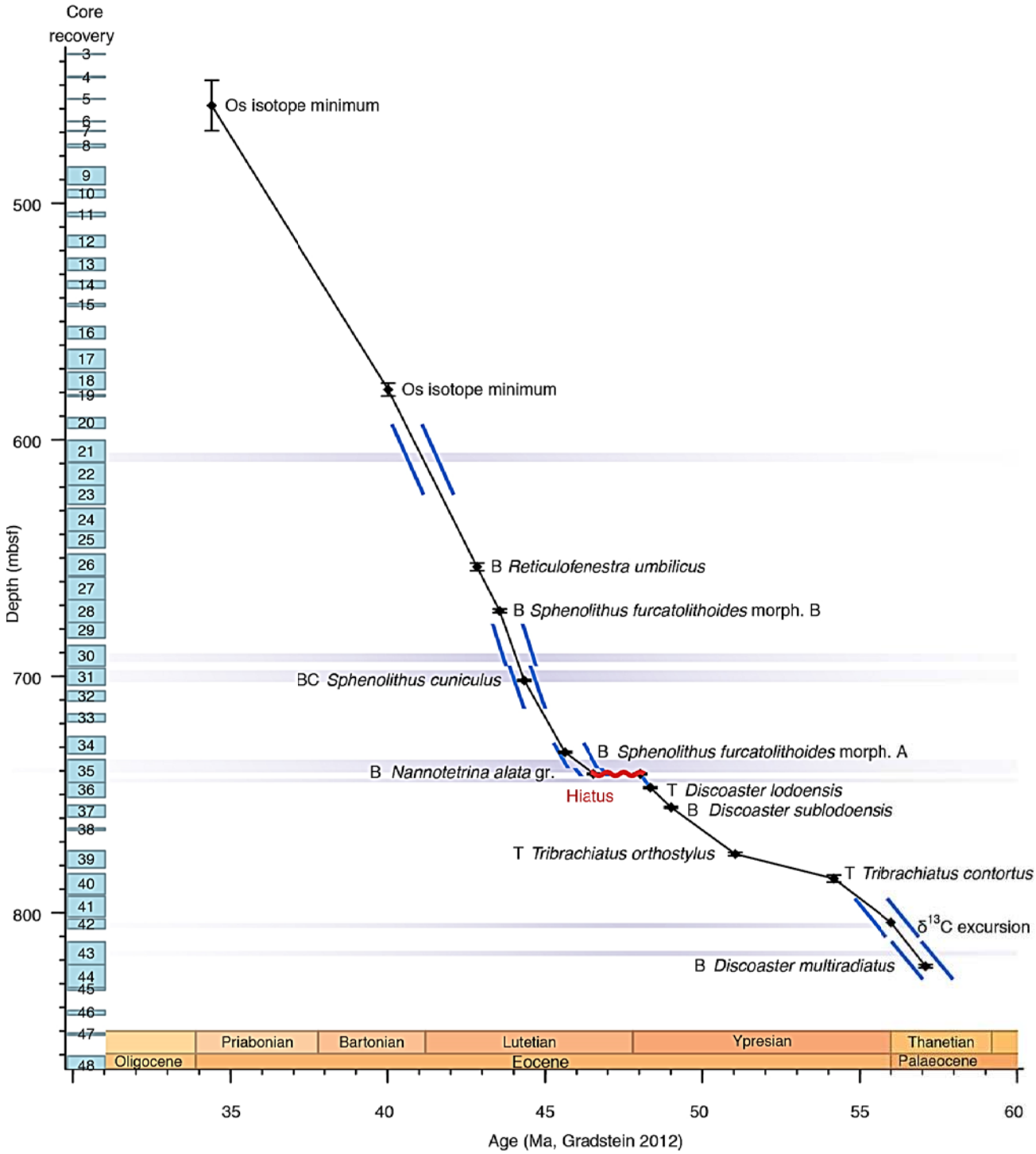
Core recovery
Os isotope minimum
Os isotope minimum
B Reticulofenestra umbilicus
B Sphenolithus furcatolithoides morph. B
BC Sphenolithus cuniculus
B Sphenolithus furcatolithoides morph. A
B Nannotetrina alata gr.
Hiatus
T Discoaster lodoensis
B Discoaster sublodoensis
T Tribrachiatus orthostylus
T Tribrachiatus contortus
δ13C excursion
B Discoaster multiradiatus
Depth (mbsf)
500
600
700
800
Priabonian
Bartonian
Lutetian
Ypresian
Thanetian
Oligocene
Eocene
Palaeocene
35
40
45
50
55
60
Age (Ma, Gradstein 2012)

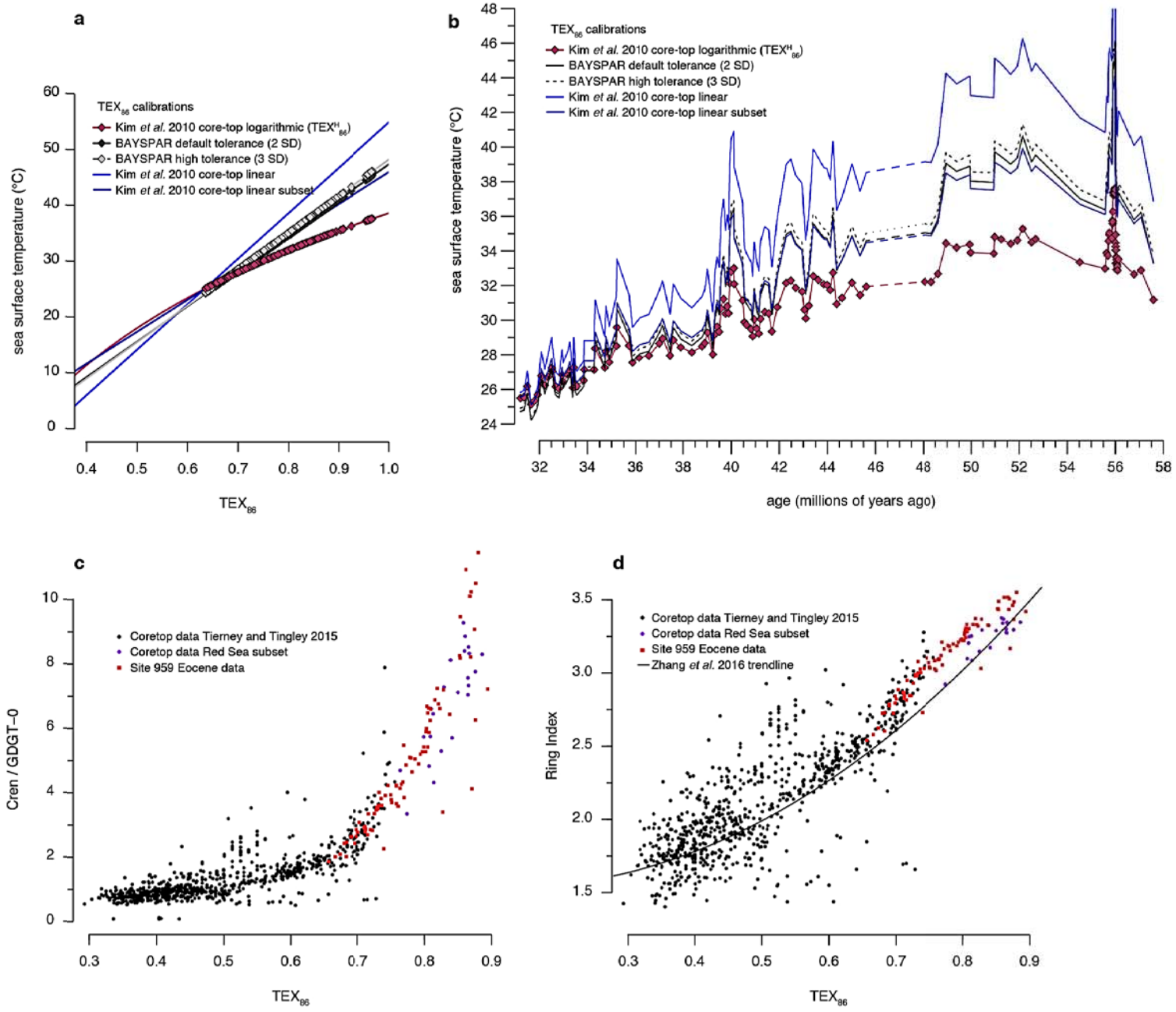
a
TEX86 calibrations
Kim et al. 2010 core-top logarithmic (TEXH86)
BAYSPAR default tolerance (2 SD)
BAYSPAR high tolerance (3 SD)
Kim et al. 2010 core-top linear
Kim et al. 2010 core-top linear subset
sea surface temperature (°C)
TEX86
b
TEX86 calibrations
Kim et al. 2010 core-top logarithmic (TEXH86)
BAYSPAR default tolerance (2 SD)
BAYSPAR high tolerance (3 SD)
Kim et al. 2010 core-top linear
Kim et al. 2010 core-top linear subset
sea surface temperature (°C)
age (millions of years ago)
c
Coretop data Tierney and Tingley 2015
Coretop data Red Sea subset
Site 959 Eocene data
Cren / GDGT–0
TEX86
d
Coretop data Tierney and Tingley 2015
Coretop data Red Sea subset
Site 959 Eocene data
Zhang et al. 2016 trendline
Ring Index
TEX86

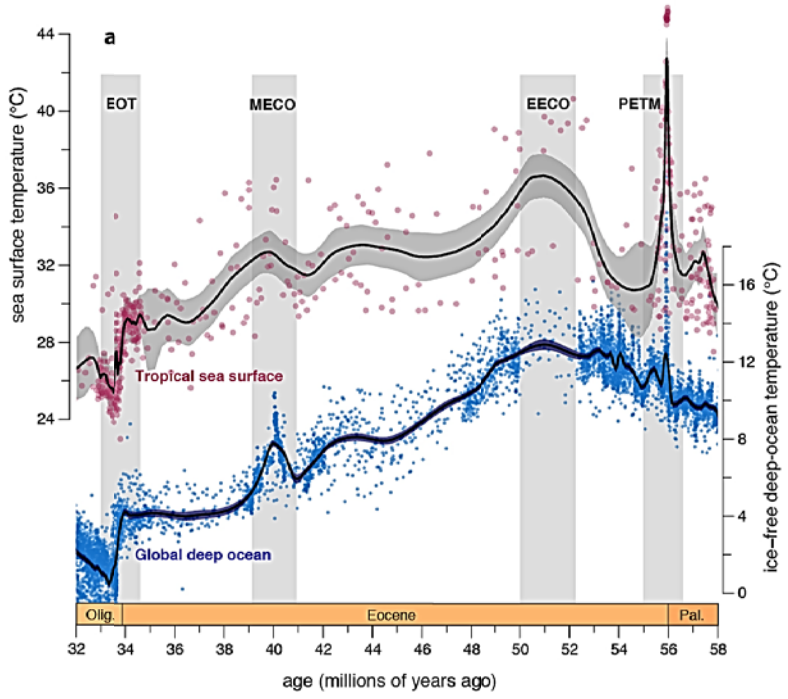
a
EOT
MECO
EECO
PETM
Tropical sea surface
Global deep ocean
sea surface temperature (°C)
ice–free deep-ocean temperature (°C)
Olig.
Eocene
Pal.
age (millions of years ago)

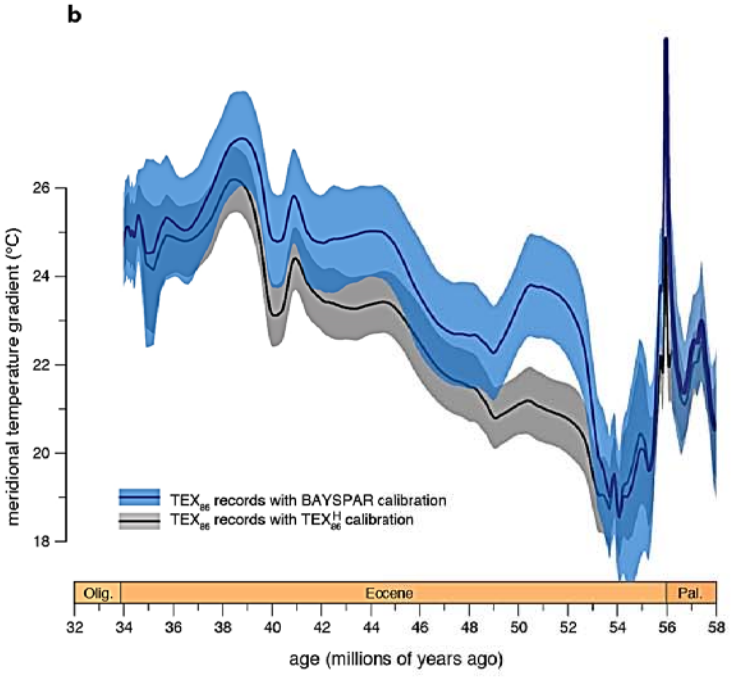
b
meridional temperature gradient (°C)
TEX86 records with BAYSPAR calibration
TEX86 records with TEX86H calibration
Olig.
Eocene
Pal.
age (millions of years ago)

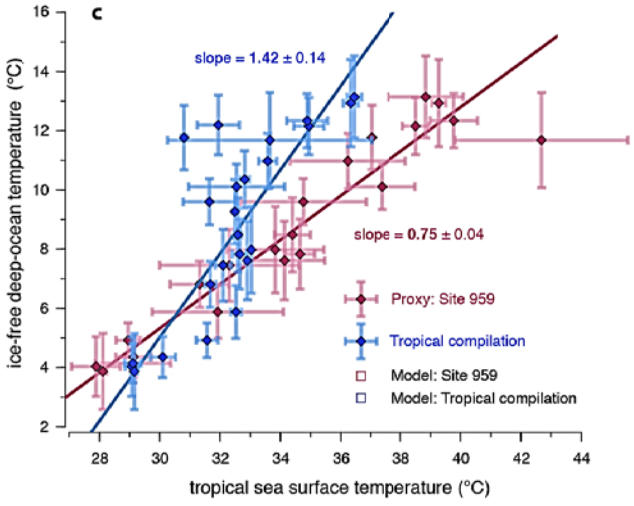
c
slope = 1.42 ± 0.14
slope = 0.75 ± 0.04
Proxy: Site 959
Tropical compilation
Model: Site 959
Model: Tropical compilation
ice-free deep-ocean temperature (°C)
tropical sea surface temperature (°C)

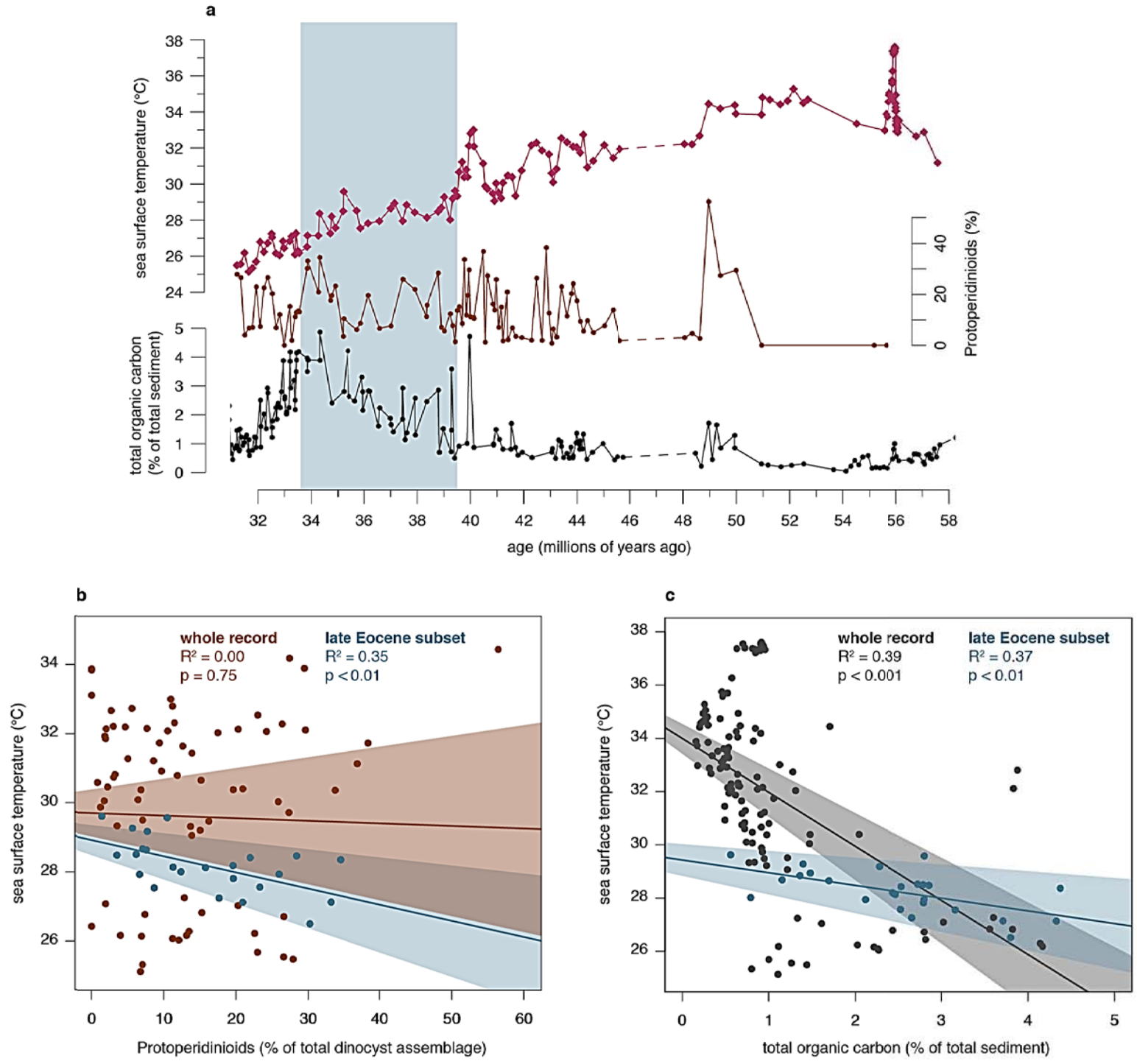
a
sea surface temperature (°C)
total organic carbon (% of total sediment)
Protoperidinioids (%)
age (millions of years ago)
b
whole record
R² = 0.00
p = 0.75
late Eocene subset
R² = 0.35
p < 0.01
sea surface temperature (°C)
Protoperidinioids (% of total dinocyst assemblage)
c
whole record
R² = 0.39
p < 0.001
late Eocene subset
R² = 0.37
p < 0.01
sea surface temperature (°C)
total organic carbon (% of total sediment)

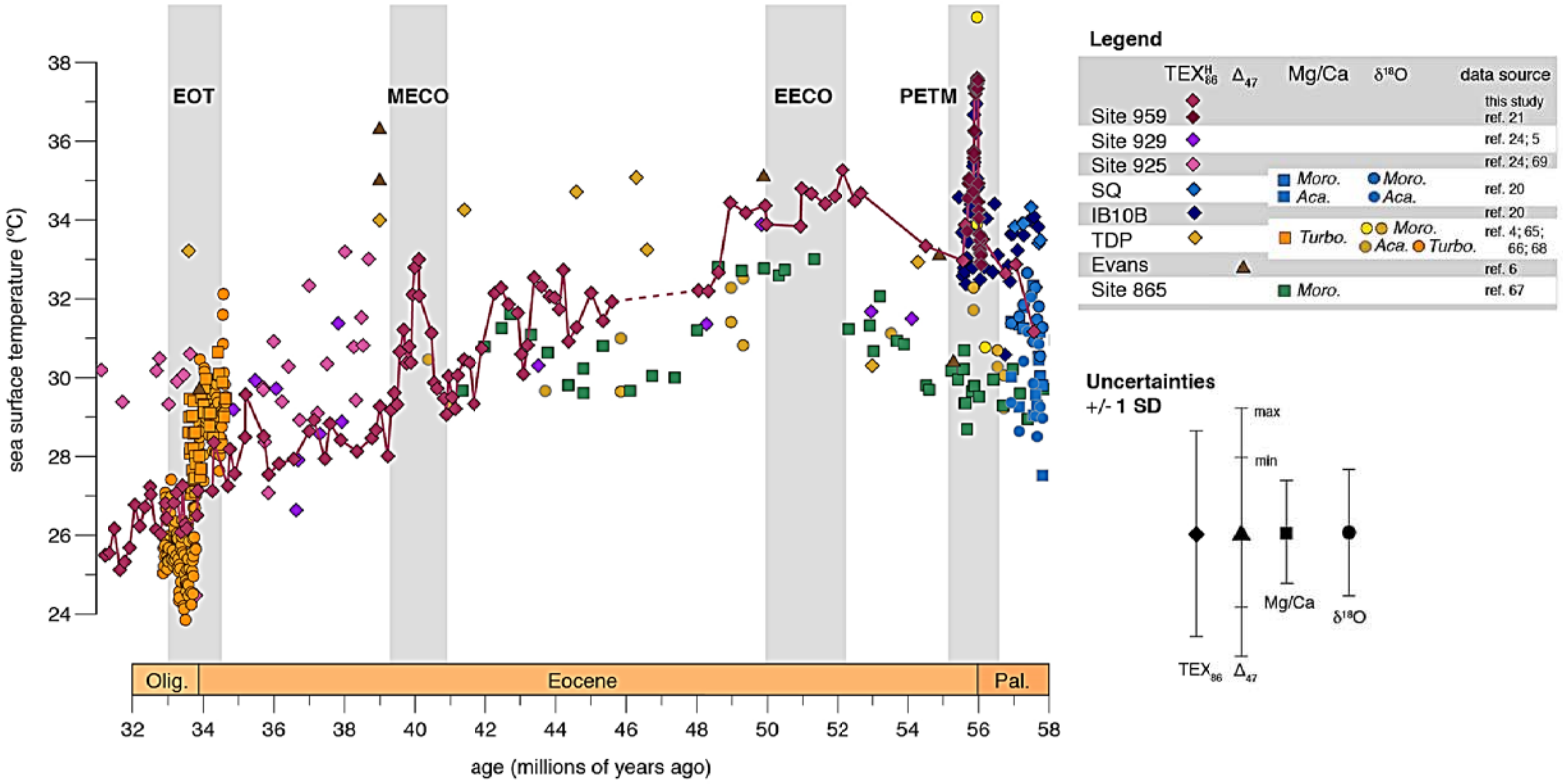
EOT
MECO
EECO
PETM
sea surface temperature (°C)
38
36
34
32
30
28
26
24
Olig.
Eocene
Pal.
32
34
36
38
40
42
44
46
48
50
52
54
56
58
age (millions of years ago)
Legend
TEX$_{86}^{H}$
Δ_{47}
Mg/Ca
$\delta^{18}O$
data source
Site 959
this study
ref. 21
Site 929
ref. 24; 5
Site 925
ref. 24; 69
SQ
Moro.
Aca.
Moro.
Aca.
ref. 20
IB10B
ref. 20
TDP
Turbo.
Moro.
Aca.
Turbo.
ref. 4; 65; 66; 68
Evans
ref. 6
Site 865
Moro.
ref. 67
Uncertainties
+/- 1 SD
max
min
Mg/Ca
$\delta^{18}O$
TEX$_{86}$
Δ_{47}

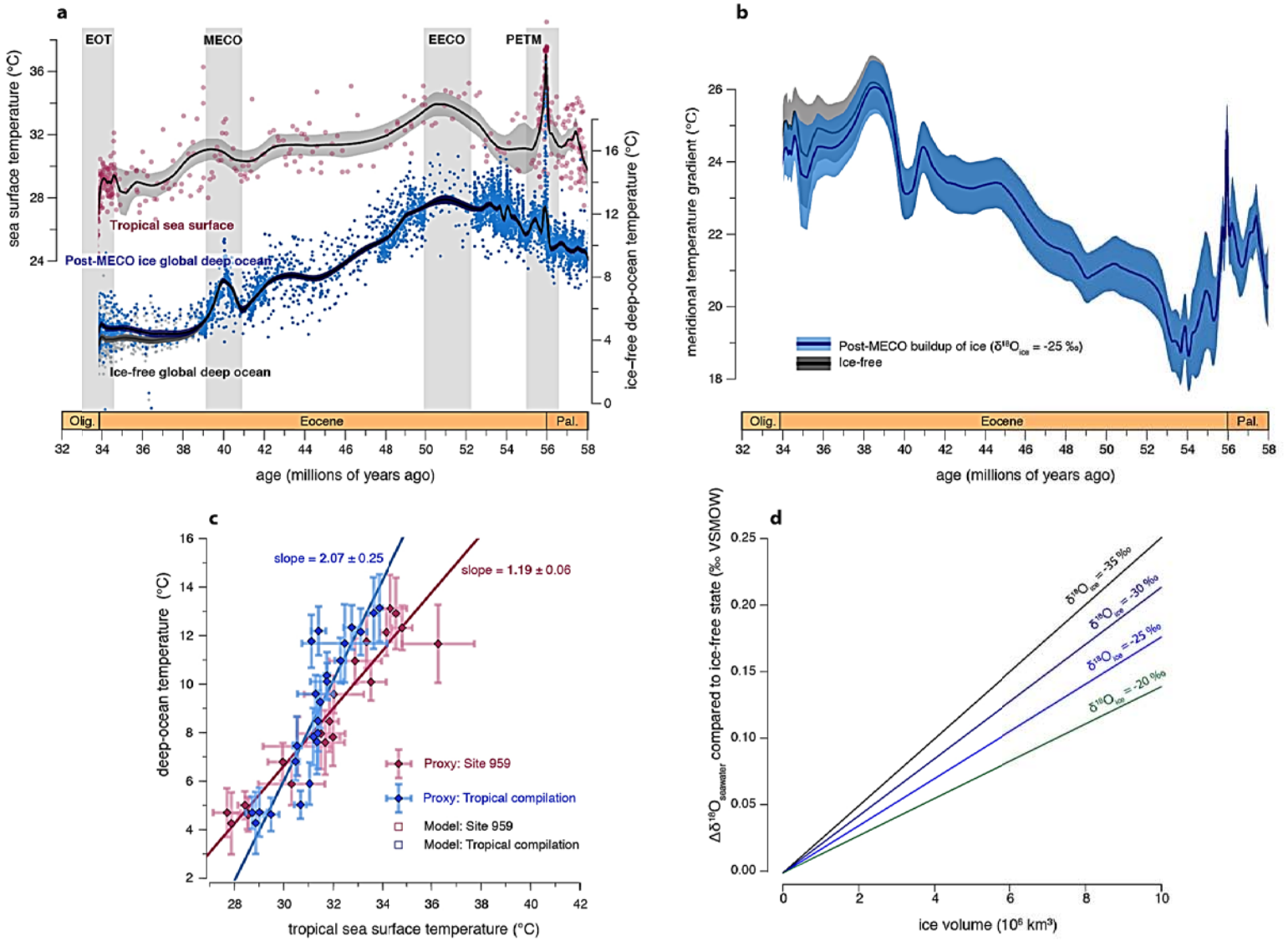
a
EOT
MECO
EECO
PETM
sea surface temperature (°C)
ice–free deep-ocean temperature (°C)
Tropical sea surface
Post-MECO ice global deep ocean
Ice-free global deep ocean
Olig.
Eocene
Pal.
age (millions of years ago)
b
meridional temperature gradient (°C)
Post-MECO buildup of ice (δ18Oice = -25 ‰)
Ice-free
Olig.
Eocene
Pal.
age (millions of years ago)
c
slope = 2.07 ± 0.25
slope = 1.19 ± 0.06
deep-ocean temperature (°C)
Proxy: Site 959
Proxy: Tropical compilation
Model: Site 959
Model: Tropical compilation
tropical sea surface temperature (°C)
d
Δδ18Oseawater compared to ice-free state (‰ VSMOW)
δ18Oice = -35 ‰
δ18Oice = -30 ‰
δ18Oice = -25 ‰
δ18Oice = -20 ‰
ice volume (10⁶ km³)

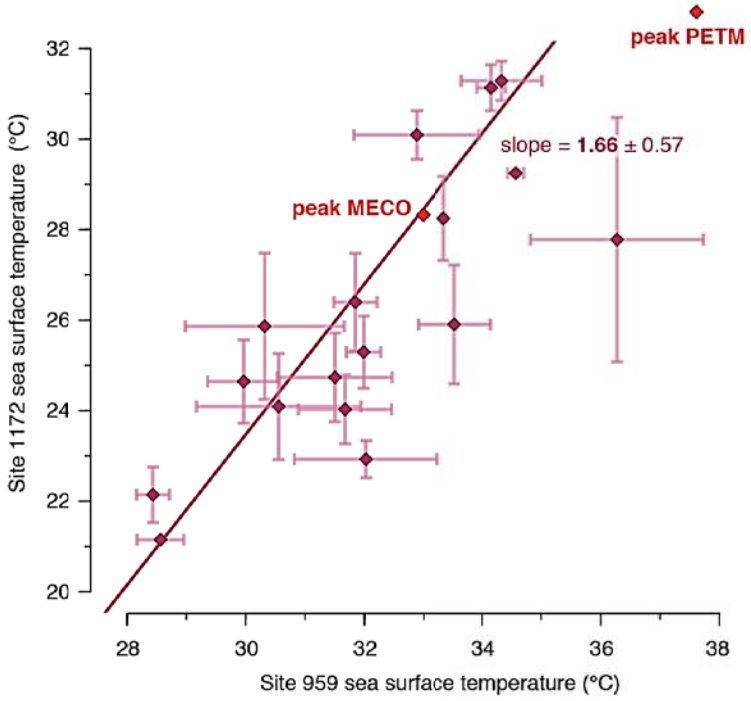
peak PETM
slope = 1.66 ± 0.57
peak MECO
Site 1172 sea surface temperature (°C)
Site 959 sea surface temperature (°C)
20
22
24
26
28
30
32
28
30
32
34
36
38

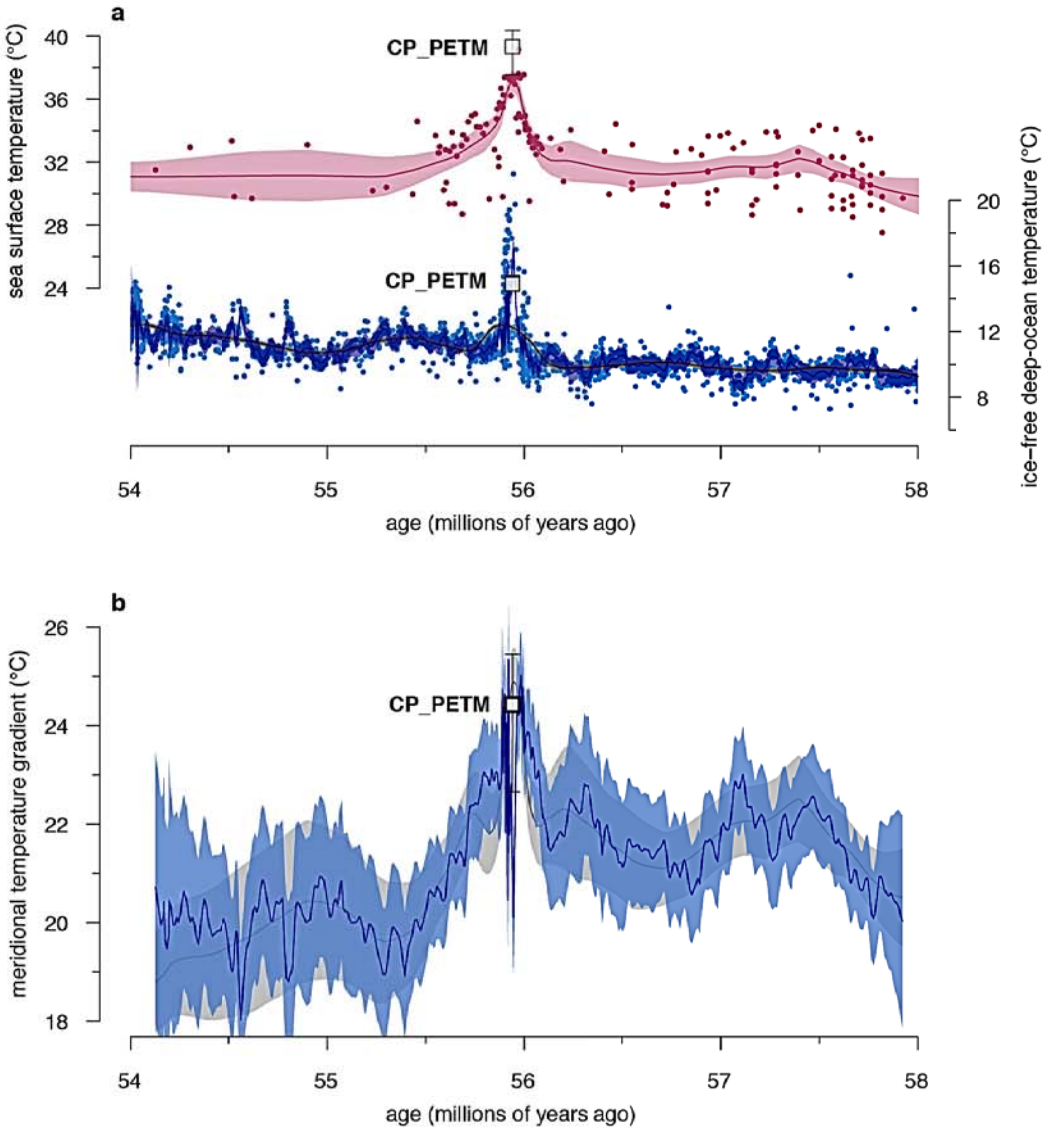
a
CP_PETM
CP_PETM
sea surface temperature (°C)
ice–free deep-ocean temperature (°C)
40
36
32
28
24
20
16
12
8
54
55
56
57
58
age (millions of years ago)
b
CP_PETM
meridional temperature gradient (°C)
26
24
22
20
18
54
55
56
57
58
age (millions of years ago)

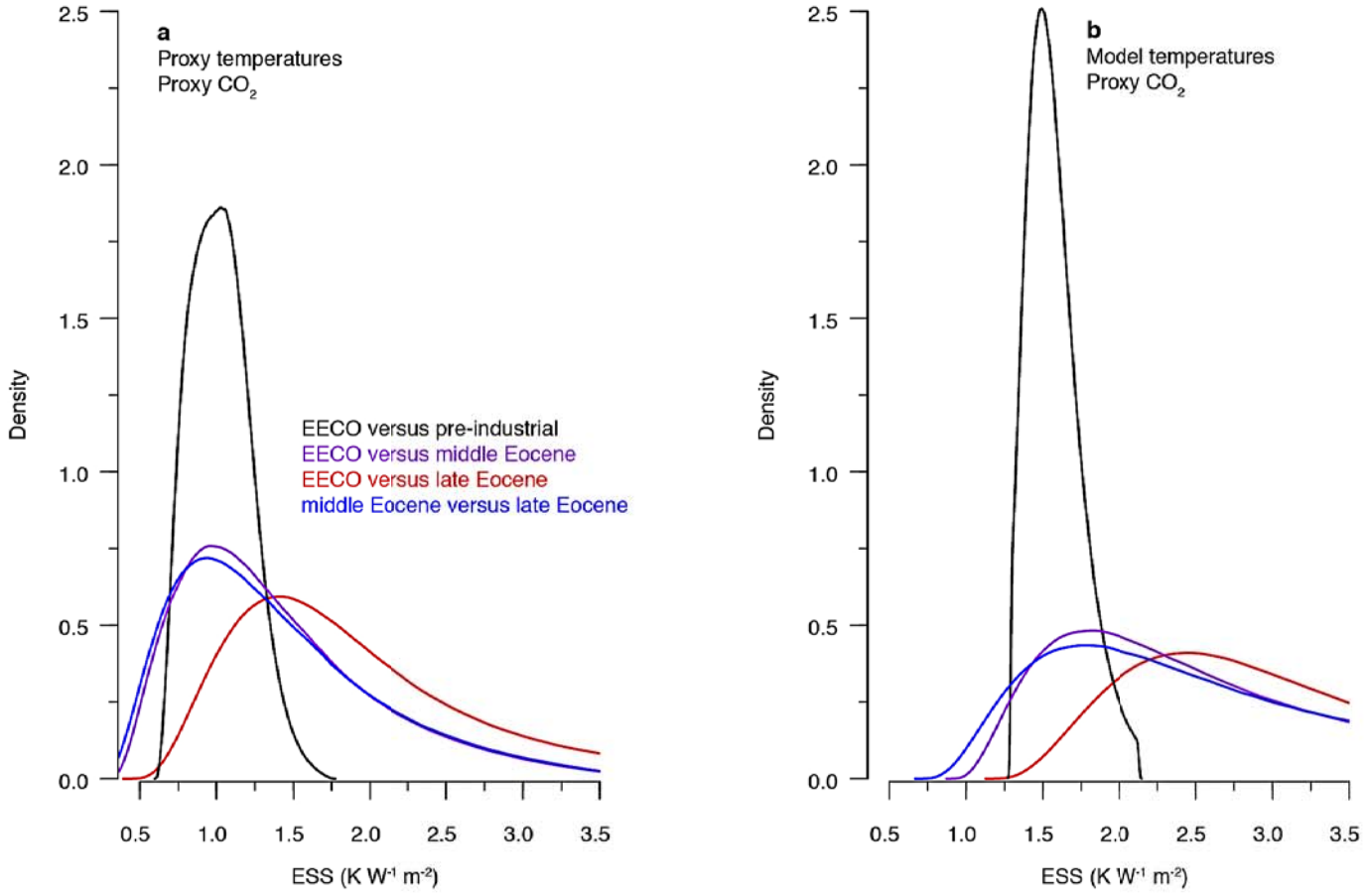
a
Proxy temperatures
Proxy CO2
EECO versus pre-industrial
EECO versus middle Eocene
EECO versus late Eocene
middle Eocene versus late Eocene
Density
ESS (K W-1 m-2)
b
Model temperatures
Proxy CO2
Density
ESS (K W-1 m-2)

a

Palaeolatitude at	Matthews *et al.* 2016	Torsvik *et al.* 2012
60 Ma	0.982 °N	9.826 °S
55 Ma	0.779 °N	9.480 °S
50 Ma	0.581 °N	9.130 °S
45 Ma	0.587 °N	7.405 °S
40 Ma	0.600 °N	5.674 °S
35 Ma	0.942 °N	4.568 °S
30 Ma	1.291 °N	3.462 °S

b

Event	Species / Proxy	Minimum depth (mbsf)	Maximum depth (mbsf)	Mean depth (mbsf)	One-sided error (m)	Age GTS2012	Reference
Latest Eocene Os isotope minimum	$^{187}Os/^{188}Os$	448.00	469.30	**458.65**	10.65	**34.40**	Ravizza and Paquay 2008([58])
MECO Os isotope minimum	$^{187}Os/^{188}Os$	576.05	581.51	**578.78**	2.73	**40.02**	van der Ploeg *et al.* in press([60])
Base	*Reticulofenestra umbilicus*	652.12	655.34	**653.73**	1.61	**42.84**	Shafik *et al.* 1998([55]); this study
Base	*Sphenolithus furcatolithoides* morph. B	671.56	673.10	**672.33**	0.77	**43.55**	This study
Base common	*Sphenolithus cuniculus*	701.38	702.12	**701.75**	0.37	**44.33**	Shafik *et al.* 1998; this study
Base	*Sphenolithus furcatolithoides* morph. A	731.73	732.49	**732.11**	0.38	**45.63**	This study
Base	*Nannotetrina alata* group	740.95	741.63	**741.29**	0.34	**46.55**	Shafik *et al.* 1998; this study
Bot hiatus	-	740.95	741.63	**741.29**	0.34	**48.03**	This study
Top	*Discoaster lodoensis*	746.73	747.45	**747.09**	0.36	**48.36**	This study
Base	*Discoaster sublodoensis*	755.06	755.80	**755.43**	0.37	**49.01**	Shafik *et al.* 1998; this study
Top	*Tribrachiatus orthostylus*	774.49	775.86	**775.18**	0.69	**51.05**	This study
Top	*Tribrachiatus contortus*	784.05	787.03	**785.54**	1.49	**54.17**	Shafik *et al.* 1998
Onset PETM isotope excursion	$\delta^{13}C$	804.08	804.10	**804.09**	0.01	**56.00**	Frieling *et al.* 2018([21])
Base	*Discoaster multiradiatus*	821.92	823.26	**822.59**	0.67	**57.10**	Shafik *et al.* 1998